JGR Oceans

RESEARCH ARTICLE
10.1029/2022JC019148

Sea Ice Production in the 2016 and 2017 Maud Rise Polynyas

Lu Zhou[1], **Céline Heuzé**[1], **and Martin Mohrmann**[2]

[1]Department of Earth Sciences, University of Gothenburg, Gothenburg, Sweden, [2]Department of Marine Sciences, University of Gothenburg, Gothenburg, Sweden

Key Points:

- Large sea ice production is found in 2016 and 2017 Maud Rise open-ocean polynyas, as large as the second largest productive coastal polynyas
- Heat flux from the upper ocean within the polynya is calculated from in-situ measurements for the first time and larger than expected
- Sea ice production within the Maud Rise polynyas is most sensitive to the choice of ice concentration products and to 1,000 hPa temperature

Supporting Information:

Supporting Information may be found in the online version of this article.

Correspondence to:

L. Zhou,
lu.zhou@gu.se

Citation:

Zhou, L., Heuzé, C., & Mohrmann, M. (2023). Sea ice production in the 2016 and 2017 Maud Rise polynyas. *Journal of Geophysical Research: Oceans*, *128*, e2022JC019148. https://doi.org/10.1029/2022JC019148

Received 13 AUG 2022
Accepted 30 JAN 2023

Author Contributions:

Conceptualization: Lu Zhou, Céline Heuzé, Martin Mohrmann
Data curation: Lu Zhou
Formal analysis: Lu Zhou, Céline Heuzé, Martin Mohrmann
Funding acquisition: Céline Heuzé
Investigation: Lu Zhou, Céline Heuzé, Martin Mohrmann
Methodology: Lu Zhou, Céline Heuzé
Project Administration: Céline Heuzé
Resources: Lu Zhou, Céline Heuzé, Martin Mohrmann
Supervision: Céline Heuzé
Visualization: Lu Zhou

Abstract Sea ice production within polynyas, an outcome of the atmosphere-ice-ocean interaction, is a major source of dense water and hence key to the global overturning circulation, but is poorly quantified over open-ocean polynyas. Using the two recent extensive open-ocean polynyas within the wider Maud Rise region of the Weddell Sea in 2016 and 2017, we here explore the sea ice energy budget and estimate their sea ice production based on satellite retrievals, in-situ hydrographic observations and the Japanese 55-year Reanalysis. We find that the oceanic heat flux amounts to 36.1 and 30.7 W m^{-2} within the 2016 and 2017 polynyas, respectively. Especially the 2017 open-ocean polynya produced nearly 200 km^3 of new sea ice, which is comparable to the production in the largest Antarctic coastal polynyas. Finally, we determine that ice production is highly correlated with and sensitive to skin temperature and wind speed, which affect the turbulent fluxes. It is also strongly sensitive to uncertainties in the sea ice concentration and 1,000 hPa temperature, which all urgently need to be better monitored at high latitudes. Lastly, more process-oriented campaigns are required to further elucidate the role of open-ocean polynya on the local and global ocean circulations.

Plain Language Summary Polynyas, openings in the sea ice, are crucial places for sea ice formation and often referred to as "ice factories." However, this ice production, which is critical to the formation of very dense and cold Antarctic Bottom Water (AABW), is rarely quantified for open-ocean polynyas. Here, we determine the sea ice volume produced within the latest 2016 and 2017 Maud Rise polynyas based on various satellite-retrieved observations by computing the heat budget throughout the ice. We also estimate the upper oceanic heat fluxes before and during a polynya from in-situ measurements within the polynya. This oceanic heat flux is crucial, as it strongly impacts ice formation. We estimate that the 2017 polynya produced an amount of ice comparable to that in the largest coastal polynyas. Finally, we find linkages between air temperature, wind speed, ocean current and our estimated sea ice formation and show that the estimation accuracy largely depends on the near-surface atmospheric and sea ice conditions. The sea ice production estimated in this study can be used to better assess the air-ice-ocean interactions in the rapidly changing polar regions, but still, more work is needed to clarify its implications for the global ocean and AABW formation.

1. Introduction

Polynyas are regions of low sea ice concentration (SIC) or thickness where the comparatively warm ocean is exposed to the cold atmosphere. Coastal polynyas are mainly driven by katabatic winds, while sensible heat convection results in open-ocean/offshore polynyas (Morales Maqueda et al., 2004). Morales Maqueda et al. (2004) (and references therein) summarized that air-ice-ocean interactions in polynyas could impact: (a) the moisture and heat exchange between atmosphere and ocean and, therefore, the local wind dynamics; (b) the upper ocean properties and vertical flows of dense saline water through brine rejection and buoyancy loss; (c) the biogeochemical fluxes, for example, acting as the sinks of atmospheric CO_2, between air and sea; and (d) the local ecosystems with extra phytoplankton and zooplankton, serving as "oases" in a polar ocean desert. In the Southern Ocean, open-ocean polynyas rarely occur but can reach a large extent. Such an open-ocean polynya, the Maud Rise polynya, opened in the vicinity of the Maud Rise seamount (centered on 64°S and 3°E) in 2016 and 2017, reaching up to 100,000 km^2 (Campbell et al., 2019; Jena et al., 2019; Swart et al., 2018). Thanks to recent advances in satellite remote sensing, the sea ice thinning of these events could be monitored (Mchedlishvili et al., 2022). As Weddell Sea polynya, it had previously reached a size of 300,000 km^2 in 1974–1976 (Carsey, 1980). In contrast, Antarctic coastal polynyas occur frequently, with a variable extent, from 130 to 20,000 km^2 (Barber & Massom, 2007).

The chain of events leading to open-ocean polynyas over Maud Rise is not yet fully understood, but it has been well-studied that their opening occurs in response to the upwelling of comparatively warm and salty Weddell Deep

Writing – original draft: Lu Zhou, Céline Heuzé, Martin Mohrmann

Water to the surface. Such upwelling has been attributed to mechanical upwelling such as Weddell Gyre spin up, Maud Rise topography, Taylor cap formation, and Ekman effects (Cheon & Gordon, 2019; D. M. Holland, 2000; D. Holland, 2001; Lindsay et al., 2004; Ou, 1991; Wilson et al., 2019; Zhou et al., 2022) and hydrostatic instabilities such as anomalous atmospheric dynamic stresses or positive energy surface flux (Campbell et al., 2019; Francis et al., 2019, 2020; A. L. Gordon et al., 2007), and induces a rapid sea ice reduction. After its opening, the polynya will remain open, changing size and position, until the heat at depth is depleted, heat loss to the atmosphere ceases, or freshwater restratifies the surface in the region (Dufour et al., 2017; T. Martin et al., 2013). However, the impact of brine rejection from sea ice production in open-ocean polynyas remains unclear and needs better quantification (Francis et al., 2020; A. Gordon, 1982). Most studies of sea ice production in the Southern Ocean have so far focused on coastal polynyas instead, which contribute as much as 10% of the total Antarctic sea ice production (Tamura et al., 2008). Moreover, ice production-related brine rejection there leads to the formation of Antarctic Bottom Water (AABW; S. Martin et al., 2007), the densest water mass that occupies the abyssal layer of the global ocean.

As polynyas are the result of air-ice-ocean interactions, sea ice thickness within polynyas can be investigated using satellites. Multiple algorithms exist to retrieve thin sea ice thickness by combining L-band microwave radiometry Soil Moisture Ocean Salinity (SMOS) and Soil Moisture Active Passive (SMAP); that is merged thin sea ice thickness product (SMOS-SMAP) from Paţilea et al. (2019). However, Paţilea et al. (2019) pointed out that this retrieved ice thickness (or "apparent sea ice thickness" (Mchedlishvili et al., 2022) instead) is only valid under the assumption that the ice concentration is near-100% and has quite large uncertainties (up to 50 cm) in low concentration.

Sea ice production within the polynya has been computed from hydrographic profiles in the Ross Sea (Thompson et al., 2020), or more commonly, using satellite-based techniques (Drucker et al., 2011; Ohshima et al., 2016; Tamura et al., 2016). However, few studies quantified sea ice production in Southern Ocean open-ocean polynyas directly from observations. Sea ice production in coastal polynyas has also been studied using coupled models (Haid & Timmermann, 2013), especially the high-resolution ones that can simulate their formation and maintenance (Marsland & Wolff, 2001) and determine the relative contribution of each heat flux, including the radiative, turbulent and ocean heat ones (Wu et al., 2003). Similar studies have been conducted for the open-ocean polynyas, generally through coupled (Timmermann et al., 1999; Walkington & Willmott, 2006) and/or high-resolution climate models (Kaufman et al., 2020; Weijer et al., 2017). Weijer et al. (2017) in particular highlighted the enhanced sensible and latent heat fluxes over the open-ocean polynyas, which, in turn, have local impacts on precipitation, cloud characteristics, and radiative fluxes, using CESM at a synoptic-scale-resolving resolution (Small et al., 2014). Some of these modeling studies also quantify the heat transfer from the ocean to the atmosphere in Southern Ocean open-ocean polynyas (Campbell et al., 2019; Kaufman et al., 2020), but more often in coastal polynyas (Haid & Timmermann, 2013; Yao & Tang, 2003). Similarly, although the role of oceanic heat on sea ice production within coastal polynyas is already described in Guo et al. (2019), few studies, be it through observations of modeling, examine its influence on open-ocean polynyas.

Therefore, in this study, we quantify sea ice production in the Maud Rise open-ocean polynyas of 2016 and 2017, from observational and reanalysis data sets. We also provide a critical analysis of the current methods and data sets available to compute sea ice production. The satellite retrievals and in-situ measurements that we use are described in Section 2, and the methods to calculate sea ice production within the polynyas as they develop are in Section 3. For the first time, when in-situ observations are available, we determine the upper oceanic heat flux within the polynya (Section 4.1). In Section 4.2, after computing the sea ice production, we investigate the local atmospheric and oceanic conditions that dominated the ice production in 2016 and 2017, respectively. We further explore the sensitivity and impacts of all input parameters that are related to the ice production calculation in Section 4.3. We then compare our results to other methods and those within coastal polynya and also address the other effects on the ice changes within the polynya in Section 5. Finally, a summary and conclusions and an outlook on future work are presented in Section 6.

2. Satellite, Reanalysis, and In-Situ Data

2.1. Sea Ice Concentration From ASI

We focus on the region of Maud Rise within the Weddell Sea between 20°W and 20°E and from 75° to 60°S, that is, the area where open-ocean polynyas occasionally form (Heuzé et al., 2021). We use the daily ARTIST Sea Ice

(ASI) Version 5 SIC (Melsheimer & Spreen, 2019; Spreen et al., 2008) with a resolution of 6.25 km × 6.25 km on a polar stereographic grid from the Advanced Microwave Scanning Radiometer 2 (AMSR2). We determine the extent of the 2016 and 2017 polynyas during the austral winter (May-October) by applying to these a standard 60% SIC threshold (Campbell et al., 2019), and "flood fill" algorithm to mask out the open ocean and the Antarctic continent, ice shelves, and adjacent coastal polynyas (Mohrmann et al., 2021). The polynya extent outlined by 60% threshold quite well matches with the image (Figure S1 in Supporting Information S1) from Sentinel-1 synthetic aperture radar after correction (Filipponi, 2019), see Text S1 in Supporting Information S1 for more information. Figure 1a shows the daily polynya area using this definition (lines) in 2016 (red) and 2017 (blue). The polynya extent variability is consistent among the different open-ocean polynya thresholds, although the more "relaxed" the threshold (e.g., 80%), the more days with a large extent. These timeseries re-demonstrate that the open-ocean polynyas mainly occurred in August and October 2016 and in September-October 2017, with a maximum extent over 100,000 km^2 during the 2017 event. For the ice production sensitivity studies (Section 4.3), we compare the results obtained with ASI to those using the relatively low spatial resolution (25 km × 25 km) SIC from two different NSIDC products, also used by Campbell et al. (2019), that is, NASA Team algorithm (DiGirolamo et al., 2022) and Bootstrap algorithm (Comiso, 2017). Despite their different resolutions, polynya extent estimation from these products and others at intermediate resolutions are highly correlated with each other and most sensitive to the product choice, not its resolution (not shown).

2.2. Radiative Fluxes From CERES-SYN

As we explain in Section 3, we compute the sea ice production via the energy budget. To quantify the radiative fluxes in the surface energy budget, we use all solar and long-wave downwelling/upwelling surface fluxes from the Edition 4 Clouds and the Earth's Radiant Energy System (CERES) SYN1deg-Day (Doelling et al., 2013, 2016) data set (hereafter referred to simply as CERES-SYN), which currently extends from 2002 until now. All CERES fluxes calculations are based on the Fu-Liou correlated-k 2/4 stream radiative transfer model (Fu & Liou, 1992) combining MODIS Terra, MODIS Aqua, and Geostationary imager satellites, meteorological profiles from the NASA Global Modeling and Assimilation Office, and surface properties from several sources providing a global 1° × 1° grid. According to Riihelä et al. (2017), the CERES-SYN data sets over the polar region fluxes show the smallest root-mean-square error against in situ fluxes over both the sea ice and the ice sheet. To achieve consistency between the computed and observed top of the atmosphere fluxes from Terra and Aqua, small adjustments are made and then labeled as "tuned" fluxes while the originally computed surface fluxes are "untuned" (Rose et al., 2013). Despite its comparatively coarse resolution, CERES-SYN performs better than the reanalysis ERA5 in estimating radiative fluxes over the ocean surface (Tang et al., 2021). Here, we use the "tuned" adjusted all-sky profile fluxes to quantify the energy budget in Section 4.2 and "untuned" initial surface fluxes to carry out sensitivity studies in Section 4.3. All fluxes are interpolated onto the ASI SIC spatial resolution.

2.3. Turbulent Fluxes From Reanalyses

To determine the turbulent flux in the energy budget, we use the method from Boisvert et al. (2020), described in Section 3.2; this method was previously applied to the satellite-based Atmospheric Infrared Sounder (AIRS; Menzel et al., 2018). We here instead complement the ASI and CERES-SYN data with the skin temperature, 1,000 hPa air temperature, 1,000 hPa relative humidity, 1,000 hPa geopotential height, and 10 m wind speeds from a reanalysis instead of AIRS due to the missing/unknown values within the polynya region during thick cloud condition. In addition, the net radiative (longwave and shortwave) and turbulent (sensible heat: SH and latent heat: LH) fluxes from four different reanalyses are also used to quantify the consistencies and discrepancies between/among different reanalyses and methods proposed in our paper.

To decide which reanalysis to use for our region, we compared four reanalysis data sets to buoy measurements: ERA5 (Hersbach et al., 2020), the Japanese 55-year Reanalysis (JRA55) (Kobayashi et al., 2015), NCEP Climate Forecast System Version 2 (CFSv2) (Saha et al., 2014), and the Modern-Era Retrospective analysis for Research and Applications, version 2 (MERRA2) (Gelaro et al., 2017). The daily snow and automatic weather station buoy measurements (Nicolaus et al., 2017a, 2017b) provide daily sea level pressure (SLP), 2 m air temperature, and relative humidity that we compared to the reanalyses. We selected the buoys that had (a) been deployed in the Weddell Sea and (b) survived at least one austral winter (40 buoys in total, Figure S2 in Supporting Information S1). Among the four reanalyses, JRA55 has the overall lowest bias and maximum correlation to all buoys

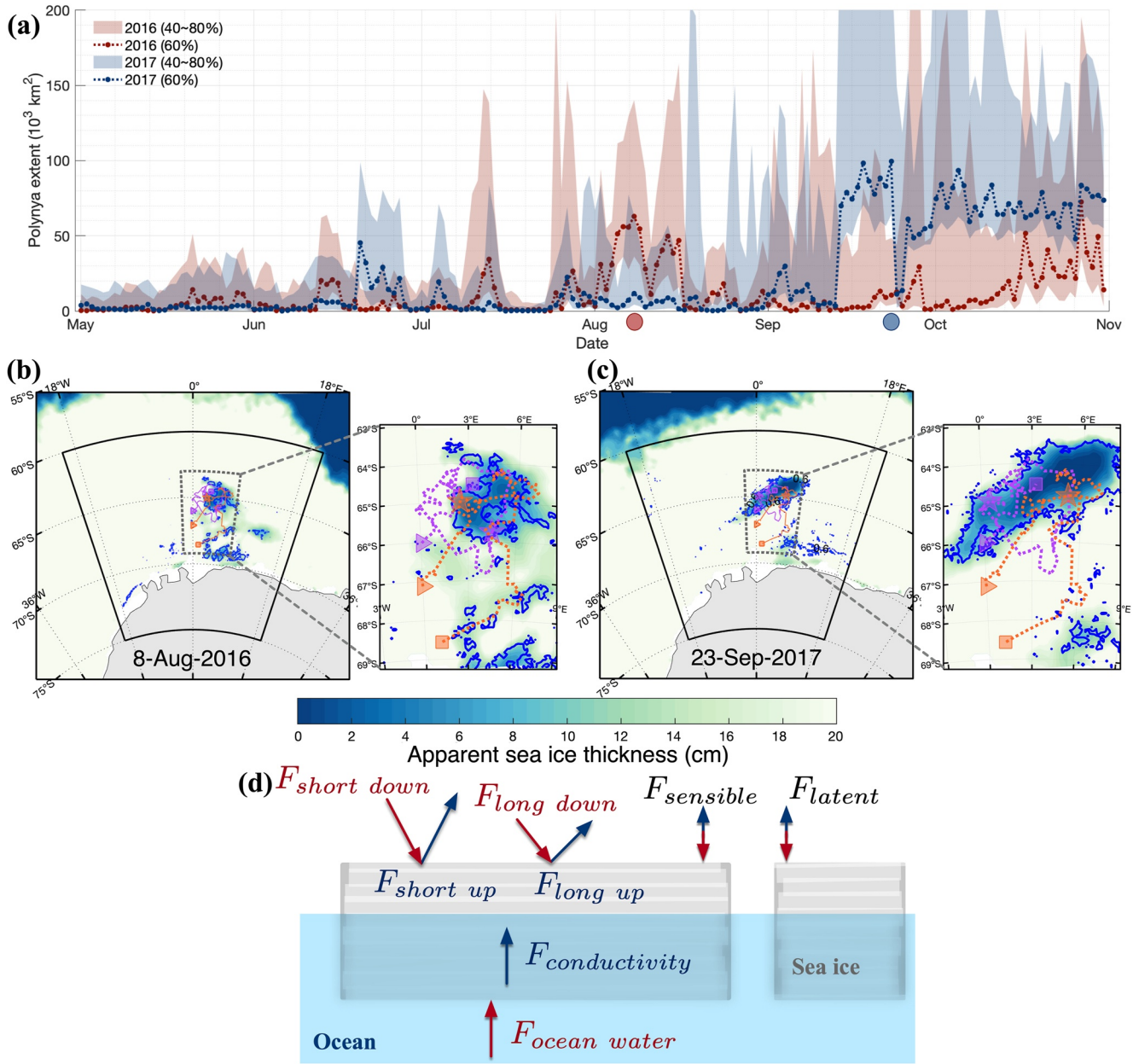

Figure 1. (a) Daily extent (in 10^3 km^2) of the polynya in 2016 (red) and 2017 (blue) based on the 60% sea ice concentration threshold (dashed lines) and within the range of 40% and 80% thresholds during the period from May to October within the wider Maud Rise region (solid lines outlined in panels (b and c)). Panels (b and c) are apparent sea ice thickness from Soil Moisture Ocean Salinity-Soil Moisture Active Passive (shadings) at the largest polynya extent day of each event on 8 August 2016 and 23 September 2017, respectively. Their dates are denoted with circles in panel (a). Orange (purple) dots are the trajectory of profiling float 5904468 (5904471) (triangle: starting on 19 January 2015 and 12 December 2014; square: ending on 14 October 2019 and 7 June 2019), identical on both panels, while the stars indicate the float location on 8 August 2016 and 23 September 2017. Right corner inset figures: zoom in the dashed lines region. (d) Schematic representation of the fluxes and energy budget throughout the sea ice, where blue (red) arrow means that the flux results in accretion (ablation) of ice. Note that the sensible and latent heat effects depend on the values.

(Figures S3–S5 in Supporting Information S1). Although ERA5 and MERRA2 also have low biases and high correlations for SLP (Figure S3 in Supporting Information S1) and the 2 m air temperature (Figure S4 in Supporting Information S1), JRA55 is the only reanalysis with a realistic relative humidity (Figure S5 in Supporting Information S1). Therefore, for the rest of this manuscript, we use the daily atmospheric variables at a 1.25° resolution from JRA55. Note that investigating the reasons for the biases of each reanalysis would be beyond the scope of this paper.

2.4. Hydrographic Data From SOCCOM Floats

We also use hydrographic measurements from two Southern Ocean Carbon and Climate Observations and Modeling (SOCCOM) floats, with the WMOIDs 5904468 and 5904471, which fortuitously sampled the 2016 and 2017 open-ocean polynyas (see their trajectories in Figures 1a and 1c). The profiling floats measure with a 10-day cycle the temperature and salinity with an accuracy of 0.005°C and 0.01 psu, respectively, binned into 2 dbar intervals above 1,000 and 100 dbar intervals for levels between 1,000 and 2,000 dbar (Riser et al., 2018). From the individual SOCCOM profiles, we determine the mixed layer depth (MLD) using a potential density threshold $\Delta\sigma_\theta = 0.03$ kg m^{-3} from the 10 dbar value (de Boyer Montégut et al., 2004; d'Ortenzio et al., 2005). Although this method is standard for the Southern Ocean, we investigate the sensitivity of our results to the use of other MLD calculation methods in Section 4.3.

2.5. Radar Freeboard From Sentinel-3A

To estimate raw sea ice mass tendency after polynya development, we also use the 20 Hz (approx. 300 m resolution) Ku-band freeboard, which is the difference between the measured surface height and the expected sea-surface height at this location and can be indirectly taken as sea ice thickness, from Level-2 Synthetic Aperture Radar Altimeter/Microwave Radiometers enhanced product. Freeboard is derived based on the heritage of the sea ice retracker implemented in the second Cryosphere Satellite (CryoSat-2) mission (EUMETSAT, 2021). As the L2 freeboard is provided along-track direction, in order to have more samples to better capture the ice surface, freeboard from Day (−5) until Day (+5) are all gathered and taken as the Day (0)'s measurements. Then, all freeboards within the 50 km outside rim of the polynya are selected to determine the development of sea ice change.

3. Methods

In this study, as has been done before for coastal polynyas (Nihashi & Ohshima, 2015; Nakata et al., 2021; Tamura et al., 2008, 2011), we determine sea ice production within the open-ocean polynyas, visible on exemplary Figure S1d in Supporting Information S1, via daily energy budgets. This energy budget is summarized on schematic Figure 1d. This section first describes the sea ice production estimation, the different terms of the energy budget, including the oceanic heat flux, and finishes with the methods for the sensitivity study of the parameters.

3.1. Sea Ice Production Estimation

In this study, we compute the daily frazil ice production rate following Macdonald et al. (2022) and Cornish et al. (2022):

$$F_{\text{conductivity}} - F_{\text{OW}} = \rho_{\text{ice}} L_{\text{ice}} \frac{\partial hi}{\partial t}, \tag{1}$$

where $F_{\text{conductivity}}$ is the upward basal ice conductivity flux that contributes to accreting the ice, F_{OW} is the ocean heat flux that in our case ablates the ice, ρ_{ice} is the ice density (= 920 kg m^{-3}), $L_{\text{ice}} = 279$ KJ kg^{-1} the latent heat of fusion for ice production determined for the Ross Sea (Cheng et al., 2017), and which we assume can be applied to the Weddell Sea, and *hi* the ice thickness. Using Equation 1 to determine $\frac{\partial hi}{\partial t}$, the daily sea ice production within the polynya (V_p) is then defined as the daily change within one grid cell:

$$V_p = \frac{tA(1 - SIC)\left(F_{\text{conductivity}} - F_{OW}\right)}{\rho_{\text{ice}} L_{\text{ice}}}, \tag{2}$$

where t (= 86,400 s) is 1 day, A (= 6.25 km × 6.25 km) is the area of a AMSR2 ice concentration grid cell, and SIC the sea ice concentration. Earlier studies have used this algorithm to analyze ice production in coastal polynyas in both hemispheres (Nihashi & Ohshima, 2015; Nakata et al., 2021; Tamura et al., 2008, 2011); we here apply it to Southern Ocean open-ocean polynyas.

3.2. Energy Balance Within the Polynya

According to West et al. (2019), the ice conductivity flux is continuous through the sea ice. Besides, surface and basal conductivity flux are similar and highly correlated (Lei et al., 2010). Thus, the upward conductivity flux is assumed to be balanced by surface net radiative and turbulent fluxes (Figure 1d), that is,

$$F_{\text{conductivity}} = F_{SW} + F_{LW} + F_{SH} + F_{LH} \tag{3}$$

where F_{SW} (F_{LW}) is the upward net shortwave (longwave) radiative fluxes from CERES-SYN, F_{SH} and F_{LH} are the sensible and the latent heat flux, and all the fluxes here are positive if upward, implying sea ice growth as a results of heat lost by the ice to the atmosphere. See Figure 1d for the possible processes that can make ice melt (red arrows) or grow (blue arrows). We now give more details about each term in dedicated subsections.

3.2.1. Turbulent Flux

Satellite-based surface turbulent flux (F_{SH} and F_{LH}) retrievals rely on the bulk aerodynamic method (Monin-Obukhov similarity theory or MOST) (Panofsky, 1984) and an iterative calculation scheme (Launiainen & Vihma, 1990) following Boisvert et al. (2022), expressed as:

$$\begin{aligned} F_{LH} &= \rho\ S_r\left[C_{Ez,i}\ L_{e,i}\ SIC\ (q_{s,i} - q_z) + C_{Ez,w}\ L_{e,w}\ (1 - SIC)\ (q_{s,w} - q_z)\right] \\ F_{SH} &= c_p\ S_r\left[C_{Hz,i}\ SIC\ (T_{s,i} - T_z) + C_{Hz,w}\ (1 - SIC)\ (T_{s,w} - T_z)\right] \end{aligned} \tag{4}$$

where ρ is the air density, S_r the effective wind speed at 10 m that accounts for the enhancement of F_{SH} and F_{LH} fluxes by wind gustiness (and differs for stable and unstable boundary layers (Taylor et al., 2018), which unstable region accounted for about 93.4% of the 2016 and 2017 polynyas), C_{Ez} (C_{Hz}) is the bulk water vapor (heat) transfer coefficient over ice (i) and water (w), $L_{e,i}$ ($L_{e,w}$) is the latent heat transfer of sublimation (vaporization) over ice (water), SIC is the sea ice concentration from ASI SIC, $q_{s,i}$ ($T_{s,i}$) is the saturation specific humidity (skin temperature) at the surface of the ice, $q_{s,w}$ ($T_{s,w}$) is the same but at the ocean surface, and q_z (T_z) is the air specific humidity (temperature) at 2 m, and c_p is the specific heat of air.

This method has regularly been applied for AIRS-based surface turbulent flux calculation (Boisvert et al., 2013, 2015; Monroe et al., 2021) with some modifications, including stable conditions and roughness lengths estimation of sea ice (Andreas et al., 2010a, 2010b; Grachev et al., 2007). The 1,000 hPa air temperature and specific humidity measured at different heights are consistently interpolated to a 2 m reference height until surface stability parameter (roughness length is divided by Monin-Obukhov length) is approaching convergence (less than 0.01). JRA55 1,000 hPa geopotential height within the Maud Rise region is normally below the surface, about −123.6 m. As mentioned in Boisvert et al. (2020), if the 1,000 hPa geopotential height is below the surface, in which case it is set to 2 m. The daily turbulent heat fluxes (LH and SH) are computed from the JRA55 inputs, after interpolating them to the same 6.25 km × 6.25 km polar stereographic grid as the sea ice.

The reader can find a more detailed description of the parameterization of these terms in Boisvert et al. (2013, 2015).

3.2.2. Oceanic Heat Flux

Similar to Ackley et al. (2020), the oceanic heat flux (F_{OW}) in Equation 1 is calculated from the float data as (Maykut & McPhee, 1995):

$$F_{OW} = \rho_w c_w C_H u_{*0} \delta T, \tag{5}$$

where $\rho_w = 1{,}024$ kg m^{-3} is a reference seawater density, $c_w = 3{,}980$ J kg^{-1} K^{-1} the specific heat capacity of seawater, $C_H = 0.0056$ the heat transfer coefficient that can be used in the Weddell Sea (McPhee et al., 1999), u_{*0} the friction velocity at the ice/ocean interface, and $\delta T = T_{\text{ML}} - T_f(S_{\text{ML}})$ the deviation of the seawater temperature from the freezing point within the mixed layer. Here, $T_f(S_{\text{ML}})$ is the freezing temperature, which was computed from salinity and pressure following the TEOS10 algorithms, as implemented in the Gibbs Sea Water toolbox (McDougall & Barker, 2011). Thus, the MLD lead to the determination of δT.

The magnitude of u_{*0} is obtained from the geostrophic drag relation as in Maykut and McPhee (1995):

$$\frac{|U_0|}{u_{*0}} = \left|\frac{1}{\kappa}\left[\log(R_{o*} - A - iB)\right]\right|, \tag{6}$$

where $U_0 = U_{\text{ice}} - U_g$ is the vector describing the ice velocity U_{ice} relative to the surface geostrophic current in the ocean U_g, $\kappa = 0.4$ the von Karman's constant, and A and B the Rossby similarity constants. $R_{o*} = \frac{u_{*0}}{f z_0}$ is the surface friction Rossby number, where f is the Coriolis parameter and z_0 the roughness length for under the ice surface. Based on Untersteiner et al. (2007), we use the constant values $A = 1.91$, $B = 2.12$, and $z_0 = 0.1$ m obtained from

the Arctic Ice Dynamics Joint Experiment stations measurements that have also been applied to the Weddell Sea (McPhee et al., 1999). Sea ice velocity (U_{ice}) is available from the NSIDC 25 km × 25 km daily sea ice drifting product through merging multiple passive microwave satellite and buoy observations (Tschudi et al., 2019). Besides, the sea ice motion (Szanyi et al., 2016) is also used to derive the ice divergence $\text{div} = \frac{\partial u}{\partial x} + \frac{\partial v}{\partial y}$ for ice dynamic effects on the ice production. For the ocean geostrophic currents (U_g), we use the near-surface (0.50576 m depth) ocean current from the daily global ocean reanalysis 2V4 (Lellouche et al., 2013) in the Global Reanalysis multi-model Ensemble Product product in 0.25° × 0.25° horizontal resolution.

3.3. Sensitivity Configuration

Uncertainties in the computation of the produced sea ice volume V_p stem mainly from (a) the bulk parameter and threshold chosen in Equations 2 and 5, (b) the radiative fluxes from CERES-SYN, and (c) the JRA55 atmospheric input. As acquiring the real uncertainties from the nonlinear heat flux calculation and the errors from the reanalysis data is near-impossible, we perform sensitivity tests to assess the relative changes in V_p when perturbing these parameters.

In Section 4.3, we therefore conduct the following perturbations on the sea ice, ocean, and atmospheric parameters:

- The SIC threshold to detect a polynya, different SIC products (NASA Team algorithm (DiGirolamo et al., 2022) and Bootstrap algorithm (Comiso, 2017)), the sea ice latent heat of fusion (L_{ice}), the ice density (ρ_{ice}), and the ocean heat transfer coefficient (C_H) are perturbed by the upper and lower values from the references;
- We compute the MLD using the other five common algorithms: temperature threshold ($\Delta T = 0.2°\text{C}$), temperature gradient threshold ($\Delta \frac{\partial T}{\partial z} = 0.005°\text{C m}^{-1}$), intersection of the mixed layer and seasonal-thermocline fits (MLTFIT: $T_{\text{MLfit}} = \text{T}_{\text{Thermfit}}$), potential density gradient threshold ($\Delta \frac{\partial \sigma_\theta}{\partial z} = 0.0005 \text{ kg m}^{-4}$), and potential-density fit ($\sigma\theta_{\text{MLfit}}$) from Holte and Talley (2009). We also quantify the effect of setting the freezing temperature of sea water to fixed thresholds (−2.0°C, −1.9°C, and −1.8°C), of sea ice drift errors from NSIDC (Tschudi et al., 2019), and ocean surface current uncertainties from GLORYS multi-model ensembles (Garric & Parent, 2018);
- CERES-SYN "tuned" data are replaced by "untuned" data (see Section 2);
- All JRA55 atm parameters are perturbed within eight scenarios (±10%, ±20%, ±50%, and ±80%) of each value.

4. Results

4.1. Oceanic Heat Flux and Energy Balance

Campbell et al. (2019) discussed deep overturning and upper ocean haline stratification in the Weddell Sea using the data from two SOCCOM floats that were sampling within the 2016 and 2017 polynyas. We here expand their study to compute the oceanic heat flux from the mixed layer within the polynyas using the same data set (Figure 2, vertical dashed lines within the polynyas labeled with the ice concentration). As noted in Campbell et al. (2019), the mixed layer becomes shallower at some time (white line, float 5904468 and 5904471 in Figures 2a and 2c), probably as a result of ocean surface freshening from ice melt (Figures 2b and 2d). The process related to the mixed layer shoaling will be discussed in Section 5.2. Meanwhile, ocean temperatures both below and within the mixed layer are above freezing while the polynya is open (positive values on Figures 2a and 2c, most clearly visible during the 2017 polynya).

Although the apparent sea ice thickness from SMOS-SMAP (purple line) decreases at the location of the floats during the polynyas, the difference in oceanic heat flux F_{OW} (green lines), calculated from the floats and Equation 5, in the presence and absence of a polynya is not statistically significant. The average oceanic heat flux along the float trajectory for the period during which SIC is lower than 60% is 36.08 Wm^{-2} during the 2016 polynya, and 30.72 Wm^{-2} during the 2017 polynya in Table 1. By combining the two floats measurements, the monthly mean oceanic heat flux is thus presented in Table 1 in 2016 and 2017, with the maximum being about 67.28 and 52.26 Wm^{-2}, respectively. These values are close to that from A. L. Gordon and Huber (1990) (41 Wm^{-2}) but larger than the annual mean oceanic heat flux in Petit and Norro (2000) (see their Figure 15), although none of these was measured in a polynya; the discrepancy will nonetheless be addressed later in this manuscript.

Through the floats measurements, we can estimate the ocean heat flux every 10 days for each float, which are not sampling in sync. We can then compute the daily mean ocean flux (thick light green lines in Figures 2b and 2d)

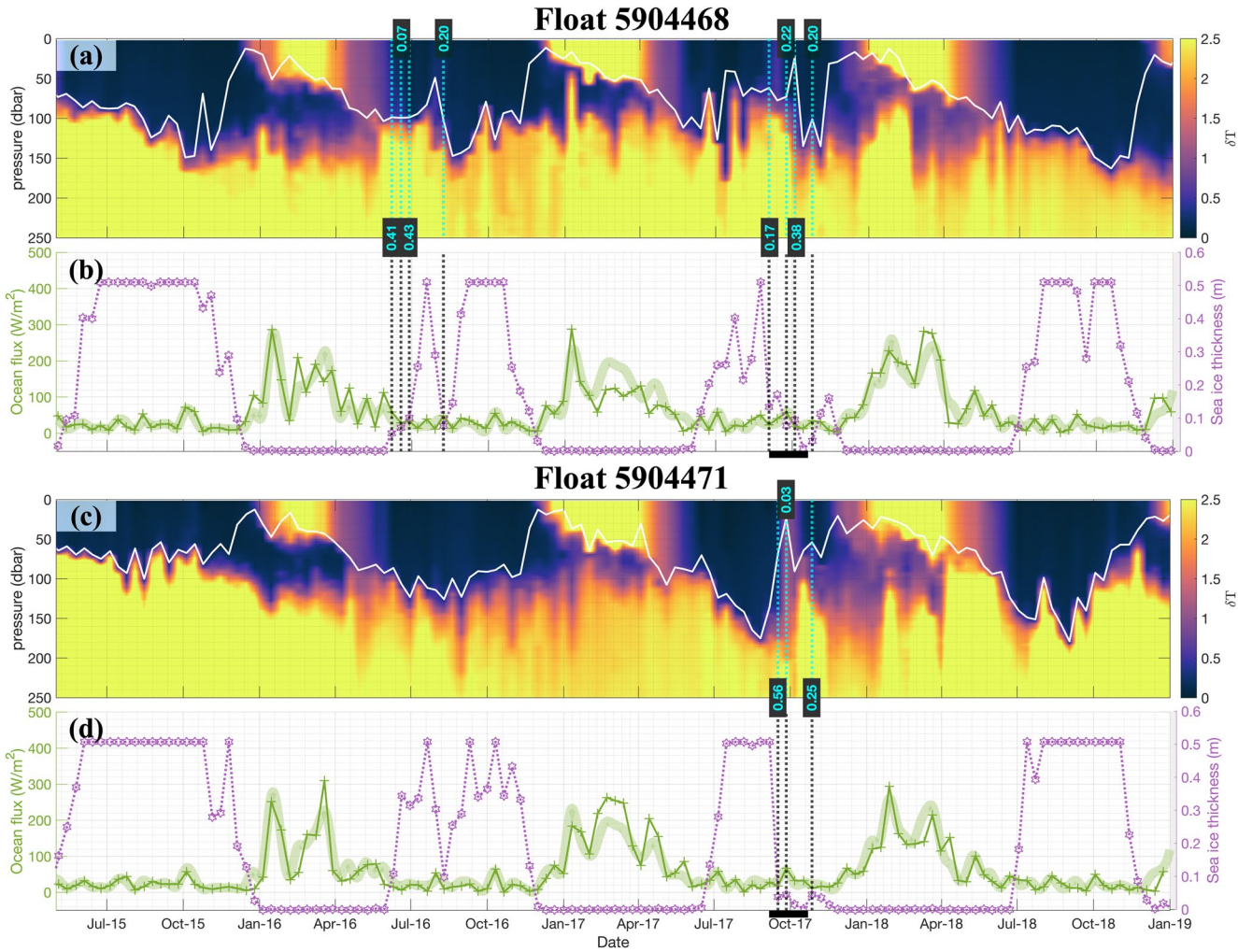

Figure 2. Time-depth sections from the profiling float 5904468 and 5904471: (a and c), temperature difference (δT, units: °C) between the measured temperature and the freezing temperature of seawater (shading), mixed layer depth (white line), and sea ice concentration (SIC) value from ARTIST Sea Ice SIC during the polynya (vertical dashed cyan line); (b and d), sea ice thickness (purple) and oceanic heat flux calculated from Equation 5 (thin green). Thick light green lines are the mean daily ocean heat flux from float 5904468 and 5904471. Solid thick line is the period discussed in Section 5.2.

by first linearly interpolating between consecutive float values for each float, and then averaging all the floats. The daily average heat energy from the ocean can then be included in the 2016 and 2017 polynya energy budget by subtracting them as in Equation 1. The result is denoted as "F + O" in the following analysis. As described in Section 3, F + O includes the radiative flux retrieved from CERES-SYN, the turbulent flux computed from the MOST method with JRA55 input, and the float-based oceanic heat flux. Figure 3 contrasts "our" (F + O) estimated flux within the 2016 and 2017 Maud Rise polynyas to the one from JRA55. Generally, the estimated flux is upward, that is, the ocean loses heat to the atmosphere, which is to be expected when sea ice is thin or open. In particular, in 2016 (Figure 3a), F + O shows an extreme heat loss (over 300 Wm^{-2}) from the ocean near the end of July, when the polynya is opening. The heat flux mainly remained upward during the entire polynya event. During the larger 2017 polynya (Figure 3b), the ocean lost over 350 Wm^{-2} heat before the polynya reached its maximum on 23 September. There were also several intrusions of heat (negative: downward) into the ocean; by the end of September, all computations agree to reveal a net downward flux of 25 Wm^{-2}.

Table 1
Mean Ocean Heat Flux (Units: W m^{-2}) From Float Observations During the Winter Months and Within the 60% Ice Concentration Regions, Denoted in Figure 2

Years	May	June	July	August	September	October	Within 60% threshold
2016	67.28	27.17	23.62	24.18	18.90	30.00	36.08
2017	52.26	23.55	32.37	22.87	41.13	23.78	30.72

The flux changes are consistent among all data sets. In fact, the computed net fluxes are significantly correlated with each other (Table S1 in Supporting

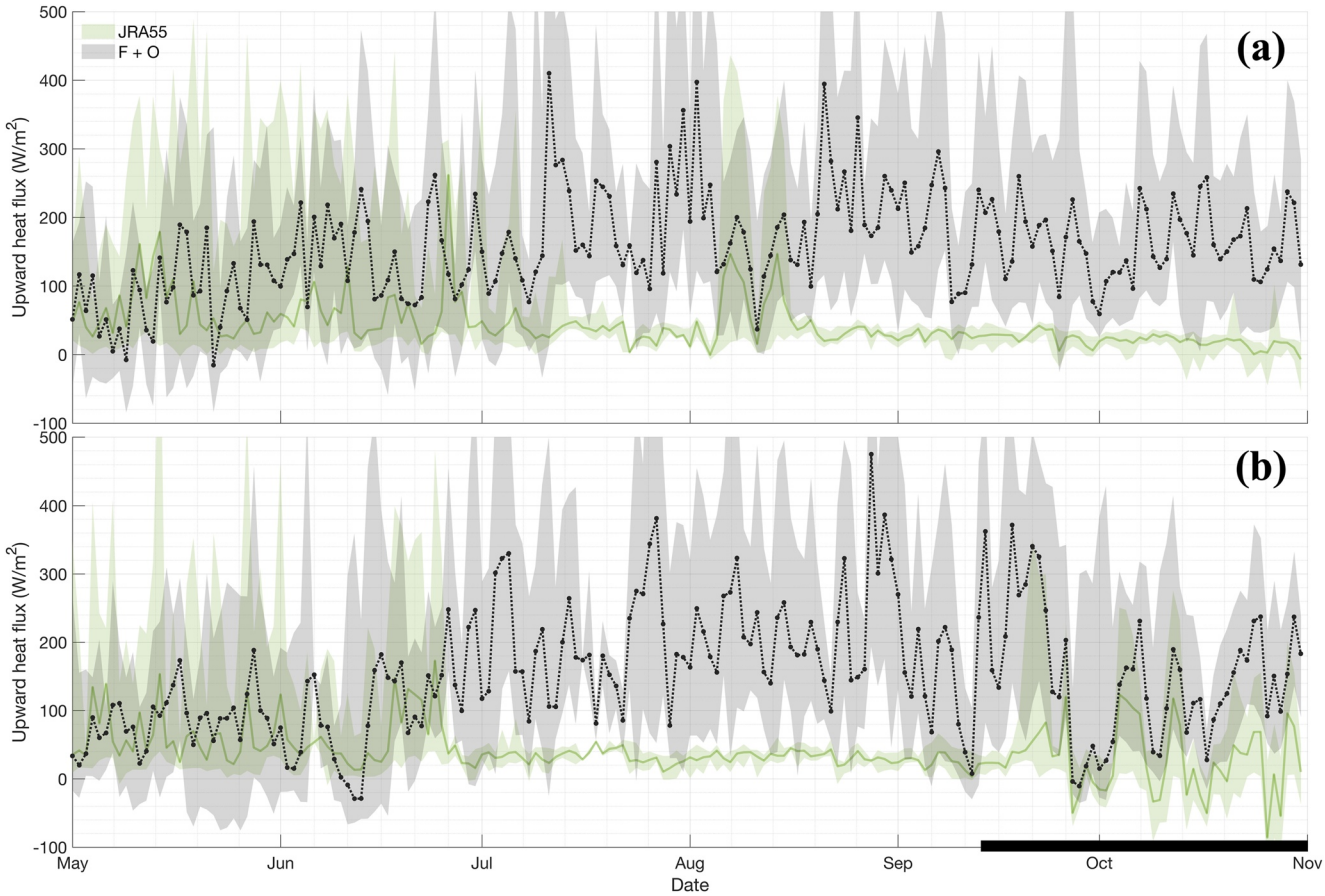

Figure 3. Daily upward heat flux (units: W m^{-2}) from JRA55 (light green) and from "F + O" (Equation 1) (gray), within the 2016 (a) and 2017 (b) Maud Rise polynyas (60% concentration threshold) during the freezing seasons (May to October). The shadings indicate the 1%–99% percentiles, and solid, and dashed lines are the mean flux value within the polynyas. Solid thick line is the period discussed in Section 5.2.

Information S1). Table S1 in Supporting Information S1 also compares the net flux calculation from F + O but with the other three reanalyses input, denoted as F + O (ERA5, CFSv2, and MERRA2) in the following. Due to the lack of partial sea-ice cover in the grid cells used by JRA55 (Kobayashi et al., 2015; Tsujino et al., 2018), those from F + O and JRA55 have the lowest correlation compared to others. The 0 or 100% sea ice treatment in JRA55 also explains that the spatial variability of net flux is the smallest in JRA55 during the freezing seasons, while the temporal variability is the largest in F + O. Nonetheless, high correlations (>0.85) between direct flux from the reanalyses and those from F + O based on those reanalyses parameters, for example, between ERA5 and F + O (ERA5), prove the robustness of the F + O algorithms.

To summarize, we computed the upper ocean heat flux when the open-ocean polynya occurred based on the floats measurements. Then, for the first time, the flux budget proposed here, F + O, also incorporates this observationally deduced flux in the heat budget over the Maud Rise open-ocean polynya. We now use this heat budget to examine the sea ice production within the two most recent Maud Rise polynya events.

4.2. Sea Ice Production in the Polynyas, and the Role of the Atmosphere and Ocean

Using the upward flux estimated from F + O, we compute the daily sea ice production through Equation 1. Figures 4a and 4b show the daily ice produced within the day of maximum polynya extent in 2016 and 2017 (the same 2 days as in Figure 1). Average (maximum) sea ice produced on 8 August 2016 is about 0.073 m (0.149 m) and reaches 0.097 m (0.179 m) on 23 September 2017. Note for both years the region-dependent distribution, in which the production is more prominent in the northern part of the polynya in response to the sensible flux released to the atmosphere (not shown).

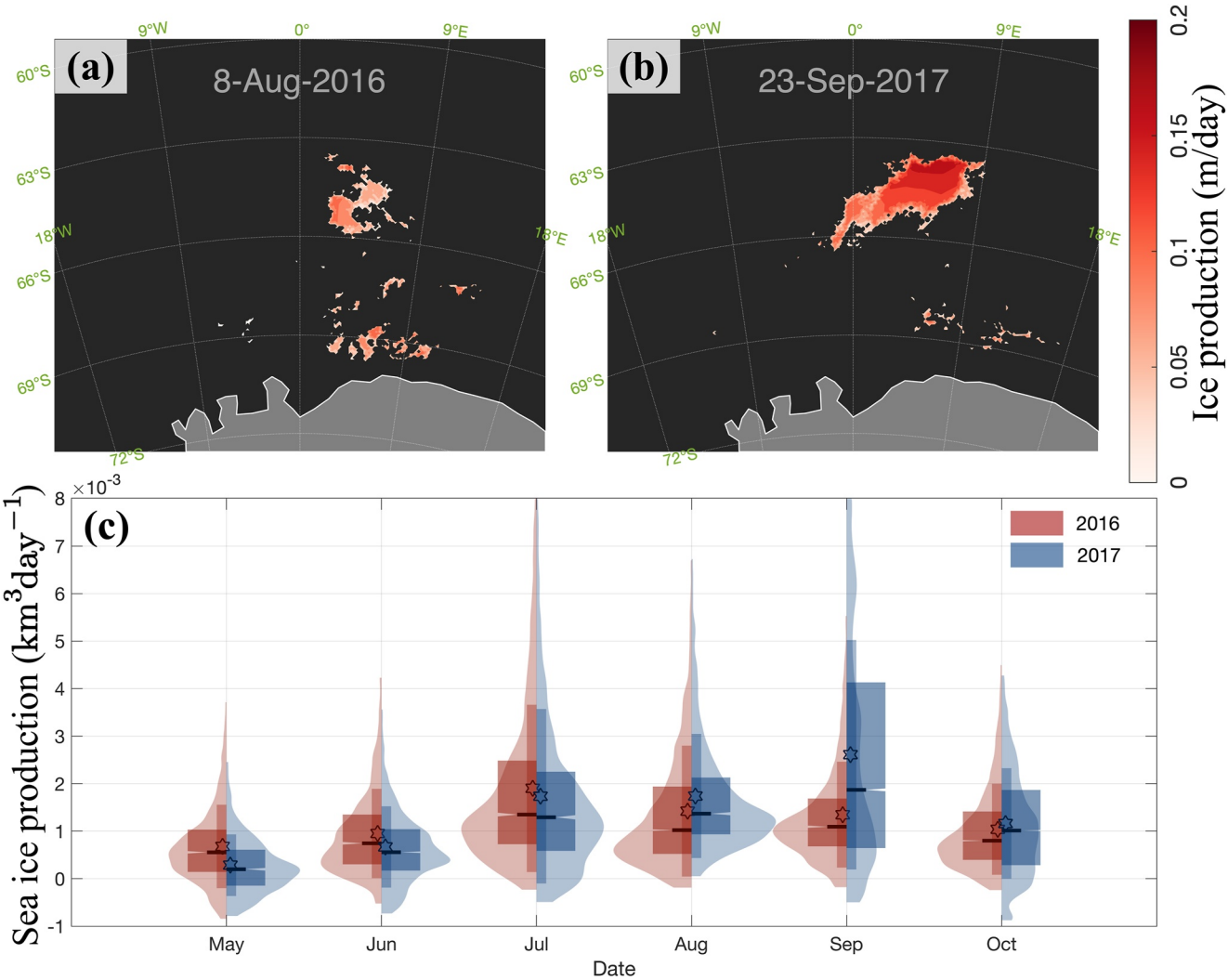

Figure 4. Spatial distribution of sea ice production on (a) 8 August 2016 and (b) 23 September 2017, that is, days of maximum polynya extent for each year (same days as in Figure 1). (c) Distribution of monthly sea ice production (units: $km^3\ day^{-1}$) from Equation 1 within the 2016 (red, left) and 2017 (blue, right) Maud Rise polynyas. The violin shadings cover the range of 1st and 99th percentiles, the upper (lower) boundaries of slim boxes are the mean ± standard deviation, while the upper (lower) ones in thick boxes are the third and first quartiles of ice production. The stars (short-solid horizontal lines) represent the mean (median) of monthly production.

The monthly distribution and the related statistical parameters of sea ice production for each cell within the 2016 (2017) polynya are shaded in red (blue) in Figure 4c. The peak production for 2016 is in July, with 1.8×10^{-3} km^3/day on average. In 2017, although the polynya has a large extent throughout October, the amount of ice produced is highest in September while the polynya grows, corresponding to the significant September heat loss (Figure 3). The average September 2017 sea ice production for each 6.25×6.25 km cell is over 2.5×10^{-3} km^3/day, with over 70% among them over 2.0×10^{-3} km^3/day. There are also negative ice production (i.e., melting) values over the wider Maud Rise (within the polynya area), mainly in May before the seasonal ice cover has fully settled and in late October as the sunlight returns. Note that the ice dynamics properties, that is, ice advection and deformation, are comparatively small and cannot explain these values, as we will show in Section 5. Finally, the accumulated ice produced during the freezing season (May to October) is summarized in Table 2: 87.50 km^3 in 2016 and 204.00 km^3 in 2017 in total within the polynyas. As we will discuss later in this manuscript, this is the same order of magnitude as produced by the largest coastal polynyas.

We further examine the relationship between daily sea ice production, near-surface atmosphere condition from JRA55, and ocean currents from GLORYS to find the determining factors for the variation of V_p (Table 2) in 2016 and 2017. As expected, we find that the sea ice production V_p is highly correlated with the polynya extent

Table 2
Determining Factors for the Variation of V_p (Table 2) in 2016 and 2017

Years	Winter ice production (km^3)	V_p vs. S_p	V_p vs. T	V_p vs. $\lvert U_{wind}\rvert$	V_p vs. $\lvert U_{ocean}\rvert$	β_T	$\beta_{\lvert U_{wind}\rvert}$	γ_T	$\gamma_{\lvert U_{ocean}\rvert}$
2016	87.50 *[15.61, 51.13]*	0.67	−0.25	0.30	0.15	−0.39	0.43	−0.32	0.24
2017	204.00 *[19.53, 183.74]*	0.40	−0.46	0.14	0.09	−0.51	0.24	−0.47	0.12

Note. 2nd column: accumulated polynya ice production (V_p) during the freezing seasons (May to October) within the key region, while the italic values in the brackets represent the $V_{apparent}$ estimation from "SMOS-SMAP" (left) and "FDD" (right). 3th–6th columns: correlation coefficient between the daily May-October ice production V_p and polynya extent (S_p), skin temperature (T), 10 m wind speed ($\lvert U_{wind}\rvert$) from JRA55, ocean surface current ($\lvert U_{ocean}\rvert$) from GLORYS, respectively. 7th–10th columns: standardized partial regression coefficients (β_T, $\beta_{\lvert U_{wind}\rvert}$, γ_T, $\gamma_{\lvert U_{ocean}\rvert}$) from two multiple linear regression analysis consisting of (a) T and $\lvert U_{wind}\rvert$, (b) T and $\lvert U_{ocean}\rvert$. All of the values are significant at the 99% confidence level.

S_p, especially in 2016 (correlation coefficient of 0.67). The volume V_p is also negatively correlated with the skin temperature (T), especially in 2017 (−0.46), and those anti-correlations dominate the north of the Maud Rise region (Figure S6a in Supporting Information S1). That is, as expected, a cold atmosphere is associated with large ice production. There is also positive correlation (Figure S6b in Supporting Information S1) between the volume of ice produced and the 10 m wind speed ($\lvert U_{wind}\rvert$) for both years, probably because the turbulent heat flux to the atmosphere is determined by T and $\lvert U_{wind}\rvert$. Correlations between ice production and ocean surface currents ($\lvert U_{ocean}\rvert$), although significant, are very small, especially in 2017 (0.09). Note that there are large uncertainties in the time series of these potential drivers, not least due to the differences in spatial resolutions, so it is no surprise that the dominating causality cannot be established. In addition, taking the dependent relationship between $\lvert U_{wind}\rvert$ and $\lvert U_{ocean}\rvert$ into account, we perform two multiple linear regression analyses in which V_p is taken as a variable explained by (a) T and $\lvert U_{wind}\rvert$, (b) T and $\lvert U_{ocean}\rvert$, respectively (Table 2). We find again that T is the dominant factor that determines V_p in the open-ocean polynyas while $\lvert U_{ocean}\rvert$ has the least influence. Interestingly, the contributions differ between the 2016 and 2017 polynyas; the wind influence on V_p is larger within the relatively small 2016 polynya, while the skin temperature clearly dominates in the large 2017 polynya. Lastly, we find that unlike ice production within coastal polynyas (Nihashi & Ohshima, 2015; Nakata et al., 2021), geostrophic winds exert a negligible influence (not shown) on the ice production in 2016/2017 open-ocean polynyas.

4.3. Sensitivity Study

As introduced in Section 3.3, we acknowledge that all parameters involved in the sea ice volume computation have inherent uncertainties that impact our results, but these uncertainties, unfortunately, cannot be obtained directly. We, therefore, instead quantify the sensitivity of V_p for the 2016 and 2017 open-ocean polynyas to perturbations of all the bulk, sea ice, oceanic, and atmospheric parameters (Table 3, Table S2 and Figure S7 in Supporting Information S1). When possible, to clarify, Table 3 also gives α, the ratio of relative changes in V_p to those in the input value.

The bulk ice parameters are varied within the ranges found in the literature (see Table 3). These include the SIC threshold for polynya determination, different ice concentration products, L_{ice}, ρ_{ice}, and C_H. Among them, the SIC products for polynya determination exert the largest impact on sea ice production, followed by the SIC threshold, with α being over 1. This is no surprise given the results of the previous section: different products or threshold changes the detected area of the polynya, which we found to be strongly correlated to V_p. Especially, both low-resolution Bootstrap and NASA Team products estimated a lower ice production in the 2016 polynya, reduced by about 35.8% and 60.8%, which could be because these low-resolution products cannot preserve small-scale ice features. Besides, the SIC Bootstrap product has been shown to overestimate the Antarctic sea ice area (Kern et al., 2019). This is likely the reason for this product to always return the smallest ice production among the three SIC products, that is, it is the one with the smallest possible polynya areas.

For the sensitivity to the oceanic terms, we notably recompute the MLD using the other algorithms/thresholds used in the literature, as well as different fixed values for the freezing point of sea water, commonly used instead of the actual salinity and pressure-dependent value. We also quantify the sensitivity to the NSIDC ice drift and GLORYS ocean currents. We find that among these, the MLD algorithm has the largest impact (Table 3): nearly 40% of the ice production in 2017 (Table S2 in Supporting Information S1) is reduced if the MLD comes from the MLFIT algorithm, that is, is computed as the intersection between the MLD and thermocline (Holte &

Table 3
Sensitivities in Accumulated May-October Polynya Sea Ice Production in 2016 and 2017 to the Input Data

Variable	Perturbed value	V_p change (%)	α
SIC threshold (%)	50 (Campbell et al., 2019)/70 (Parmiggiani, 2011)	−19.0/21.2	1.14–1.27
SIC algorithms	NASA Team algorithm (DiGirolamo et al., 2022)/Bootstrap algorithm (Comiso, 2017)	[−35.8, 22.6]/[−60.8, −18.2]	–
L_{ice} (J kg^{-1})	276 (Yu & Rothrock, 1996)/334 (Nihashi & Ohshima, 2015)	1.1/−16.5	0.83–1.01
ρ_{ice} (kg m^{-3})	900 (Tamura et al., 2008)/950 (Jardon et al., 2014)	2.2/−3.2	≈1.0
C_H	0.005/0.006 (McPhee, 1992)	[5.82, 3.52]/[−3.9, −2.35]	0.33–0.55
Mixed layer depth[a] (m)	ΔT; $\Delta\frac{\partial T}{\partial z}$; $\Delta\frac{\partial \sigma_\theta}{\partial z}$; $T_{MLfit} = T_{Thermfit}$; $\sigma\theta_{MLfit}$ (Holte & Talley, 2009)	−39.10 to 6.37	–
Freezing temperature of sea water[a] (°C)	−2.0(Thurman, 2002); −1.9(Wetzel et al., 2004); and −1.8(Hunke et al., 2017)	−4.32 to 7.6	–
NSIDC sea ice drift[a] (m s^{-1})	Error variance (Tschudi et al., 2019)	−8.8 to 1.69	–
GLORYS ocean current[a] (m s^{-1})	Multi-model ensemble uncertainties (Garric & Parent, 2018)	−1.54 to 2.03	–
CERES-SYN	"Untuned"	[−0.73, 1.94]	–
T_{skin} (°C)	−80%, −50%, −20%, −10%/10%, 20%, 50%, and 80%[b]	2.82 to 52.63/−40.97 to −2.74	0.27–0.66
$T_{1000\ hPa}$ (°C)		−123.14 to −14.15/14.34 to 151.04	1.41–1.89
Geopotential height (m)		0.23 to 5.81/−1.49 to −0.19	0.01–0.07
Relative humidity (%)		3.23 to 31.69/−30.66 to −3.23	0.32–0.40
Wind speed (m s^{-1})		−60.13 to −6.07/6.01 to 54.68	0.69–0.75

Note. Sensitivities in accumulated May-October polynya sea ice production in 2016 and 2017 to the input data, including sea ice concentration (SIC) threshold, SIC different algorithms, sea ice latent heat of fusion (L_{ice}), sea ice density (ρ_{ice}), ocean heat transfer coefficient (C_H), the other five algorithms for mixed layer depth definition ($\Delta T = 0.2$°C; $\Delta\frac{\partial T}{\partial z} = 0.005$°C m^{-1}; $\Delta\frac{\partial \sigma_\theta}{\partial z} = 0.0005$kg m^{-4}; $T_{MLfit} = T_{Thermfit}$; $\sigma\theta_{MLfit}$), freezing temperature of sea water, NSIDC sea ice drift, GLORYS ocean current, radiative flux from "untuned" CERES-SYN, and five atmospheric variables from JRA55 The slash's left and right sides are each input's lower and upper perturbation. The respective production changes for 2016 and 2017 polynyas are shown in brackets. The literature in which they were used is also cited. When meaningful, α is the ratio of V_p changes (units: %) over the perturbed changes (units: %).

[a]Detailed ice production changes (units: %) for each parameter perturbation can be found in Table S2 in Supporting Information S1. [b]Detailed ice production changes (units: %) for each parameter can be found in Figure S7 in Supporting Information S1.

Talley, 2009). The MLFIT algorithm suggests the average MLD is 28.2 m deeper in 2017, corresponding to over 70% extra heat storage in the upper ocean. However, Holte and Talley (2009) showed that this method might misidentify the thermocline in profiles from the polar regions. Overall, compared to the potential density threshold, the gradient threshold algorithms for both temperature and density always obtain a larger ice production, while those based on the fit algorithm tend to produce significantly less ice.

The sensitivities from all atmospheric parameters are considered through changing into "untuned" CERES-SYN data or proportionally increasing/decreasing the JRA55 input. The sensitivity results show that the most substantial impact arises from the temperature at 1,000 hPa (α of 1.41–1.89). That is, 1% of temperature changes can at least result in 1.4% of ice production variation (see e.g., 2016 on Figure S7 in Supporting Information S1). This is no surprise considering that in the previous paragraph, we found that sea ice production was most strongly correlated to near-surface skin temperature. Generally, the most dominant factor for ice production is near-surface (1,000 hPa) temperature, followed by SIC product, wind speed, and skin temperature.

5. Discussion

5.1. Comparison of the Methods for Sea Ice Production

The method we used here to compute sea ice production is the most commonly used for Antarctic coastal polynyas, but it is not the only method. Sea ice production can also be estimated from the "freezing degree days" (FDD) or simply by comparing day-to-day changes in SMOS-SMAP thin ice thickness, despite the large uncertainties in this product (Ludwig et al., 2019), see Text S2 in Supporting Information S1. Here, we will use the term apparent "sea ice change" ($V_{apparent}$) instead of "sea ice production" for the above FDD and SMOS-SMAP methods for less ambiguity. Preußer et al. (2019) pointed out that flux-deduced sea ice production, for example, F + O, is typically regarded as a potential upper limit for thermodynamically induced ice changes.

We compare these three methods in Figure S8 in Supporting Information S1: red and blue shadings are from our F + O estimation, identical to Figure 4; purple lines are for the FDD sea ice and green lines for the SMOS-SMAP one. Sea ice changes from SMOS-SMAP are much smaller than from the other two methods, with monthly means hardly above 0 even in 2017. The result is the same when accumulated over the entire May-October season (second column in Table 2 and dotted shadings and circle lines in Figure 6): V_{apparent} from SMOS-SMAP (square bracket, left) is only 19.5 km^3 in 2017, while that derived from FDD (square bracket, right) and F + O (no bracket) are comparable, over 50 km^3 in 2016 and over 180 km^3 in 2017. This result can partly be explained by the definition of these two auxiliary methods. The FDD estimation constantly accumulates values. Thus, the daily V_{apparent} is always positive, that is, ice can only grow with this method. In contrast, most of the SMOS-SMAP V_{apparent} is negative, indicating half of the sea ice melts during the occurrence of the polynya, which is in agreement with the oscillations in heat fluxes from Figure 3. Considerable uncertainties exist in the SMOS-SMAP product (Paţilea et al., 2019), up to 30 cm. Its current retrievability limit of 50 cm also hampers its use for sea ice volume change studies. Therefore, although the consistency between potential ice production and actual sea ice changes cannot be definitely verified, our results provide an uppermost limit of ice production, which can impact the sea ice budget in general.

5.2. Dynamics Inside the Polynya

Another significant contributor to the sea ice budget in the polynya is the sea ice motion. Sea ice convergence from outside the polynya into the polynya causes a net ice gain for the polynya, while ice divergence out of the polynya causes a net ice loss. Several studies compared the contribution of the ice-related dynamic and thermodynamic processes changing sea ice area in the Weddell Sea (P. R. Holland & Kwok, 2012; von Albedyll et al., 2022). In particular, based on a concentration budget analysis, P. R. Holland and Kwok (2012) found that during a typical freezing season, SIC over Maud Rise (named King Håkon Sea in their paper) is mainly controlled by the sea ice thermodynamic component. Huot et al. (2021) found a similar result in the polynya in their 5 km sea ice-ocean model. Besides, unlike coastal polynyas that are controlled by ice dynamic processes (katabatic wind and latent heat), open-ocean polynyas are dominated by sensible fluxes melting, that is, ice thermodynamics. Finally, the insignificant correlation between V_p and geostrophic wind, which is correlated with the ice motion in Section 4.2, also supports the hypothesis of a minor impact from the ice dynamics.

Nonetheless, we quantify the relative contributions from ice thermodynamic and dynamic processes in the ice production/volume changes during the development of the 2017 Maud Rise open-ocean polynya, largest of the two events. We here show only the period September-October 2017 (49 days in total), which exhibited the largest changes in sea ice production and polynya area. Here, in a very simple case, we first focus on the sea ice horizontal transport/advection and consider the "free drift" condition in which the rheology term, ridging redistribution, and internal force are neglected. See more computation details in Text S3 and Figure S9 in Supporting Information S1. We find that the 49 days of accumulated daily ice volume changes due to ice advection computed from the NSIDC sea ice drift data (∼5.6 km^3) is only 30% of the total sea ice volume change over the same period (∼18.5 km^3). This estimation is but an approximation, owing to the low resolution of the sea ice drift data set (25 km × 25 km here) and its uncertainties. We expect that the new daily sea ice velocity data sets from the proposed "swath-to-swath" algorithm (Lavergne et al., 2021), combined with more accurate sea ice thickness retrievals from satellites, will reduce the uncertainty of that estimation.

Then, to study other ice dynamic effects after the sea ice growth within the polynya, we further consider the ice divergence/convergence conditions (possible ridging redistribution), near the rim of polynya in Figure 5. Applied to the same 2017 polynya case study, the whole region (see animation in Movie S1) is ice divergence-dominated, without a significant trend or bias compared to the 1979–2021 climatological mean (Figure 5a). Besides, the freeboard close to the polynya does not show different tendencies between the divergence or convergence regions (Figure 5b). In particular, freeboard does not consistently increase in converging regions, further suggesting that dynamics is not the lead driver of sea ice growth. The freeboard in the divergence area presents a mild thinning trend (statistically significant only at a 90% confidence level), but it may be because the majority of the polynya region was divergence-dominated in 2017 (see Movie S1) rather than an actual dynamics effect on sea ice.

Although the true extent of the dynamics contribution cannot be quantified without higher resolution sea ice drift products, our results, in agreement with past literature (P. R. Holland & Kwok, 2012; von Albedyll et al., 2022), suggest a minor contribution of dynamics compared to thermodynamics. Therefore, after sea ice grows, produced

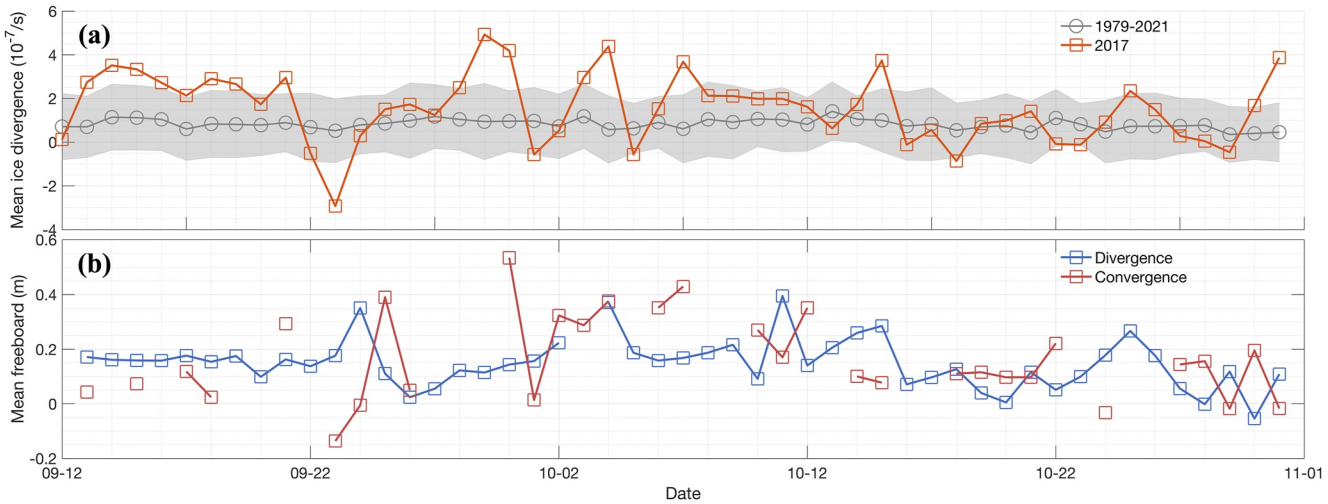

Figure 5. (a) Regional mean ice divergence in 2017 (orange) and during 1979–2021 (mean in gray line and inter-annual variability in gray shading). (b) Mean radar freeboard from Sentinel-3A within the 50 km outer rim of polynya in divergence (blue) and convergence (red) area in 2017 polynya case. See Movie S1 for polynya extent and ice divergence changes.

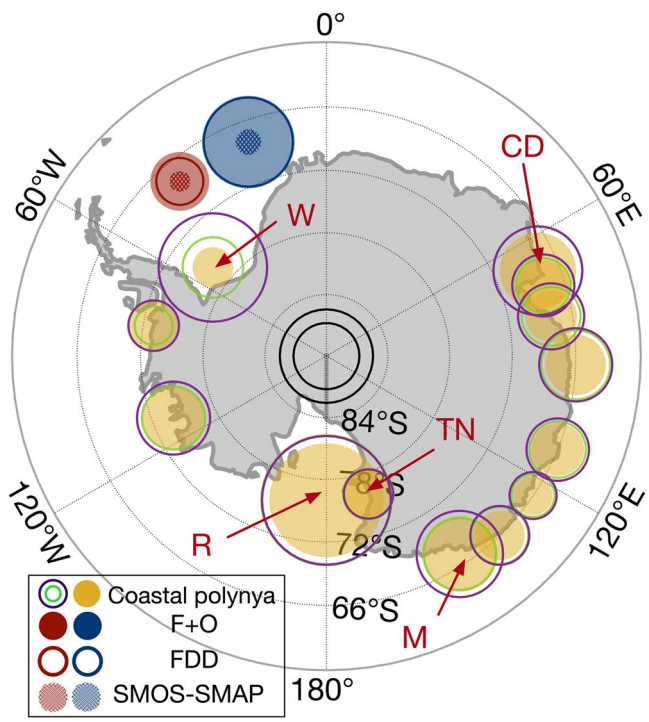

Figure 6. May to October accumulated polynya ice production within the Maud Rise region in 2016 (red) and 2017 (blue) from all three methods; "F + O" in plain circles, "freezing degree days" (FDD) in solid circles lines and "Soil Moisture Ocean Salinity-Soil Moisture Active Passive" (SMOS-SMAP) in dotted areas. The yellow patches represent the mean coastal polynya ice production between 2003 and 2010 (March to October) from Nihashi and Ohshima (2015, Table 1), the green circle lines are the estimation between 1992 and 2001 from Tamura et al. (2008, Table 1), while the purple circle lines are the estimation between 1992 and 2013 from Tamura et al. (2016, Table 1). The centered small (large) white circle corresponds to 100 (200) km^3 ice production. (W for Weddell Sea, CD for Cape Darnley, M for Mertz, TN for Terra Nova Bay, and R for Ross Ice shelf.)

transient sea ice within the polynya most likely thermodynamically melts there due to the continuous ventilation of warm sub-thermocline waters, which helps to maintain the polynya that undergoes cycles of partial sea ice melt and regrowth during the whole opening period. This process would agree with the findings in Wilson et al. (2019). They suggested that, especially over the Maud Rise, the combination of weak upper-ocean stratification and relatively strong thermocline facilitates high rates of winter ventilation and a strong negative feedback on winter ice growth. Furthermore, the entrainment of heat into the mixed layer could melt about 35% of the initial sea ice formed there.

5.3. Discussion of the Oceanic Heat Flux Estimation

As explained in for example, Guo et al. (2019), sea ice production in open-ocean polynyas is reduced by the upwelling of oceanic heat flux from the comparatively warm, modified Circumpolar Deep Water. We here estimated the oceanic heat flux directly from observations collected by drifting profilers, focusing on the heat contained within the mixed layer (up to 200 m in Figure 2).

Previous studies have found that the average upper-ocean heat flux in the western Weddell Sea varies from 7 W m^{-2} (Lytle & Ackley, 1996) to 41 W m^{-2} (A. L. Gordon & Huber, 1990) during autumn and early winter. Over Maud Rise, in particular, McPhee et al. (1999) found about 23 W m^{-2} during the ANZFLUX crewed drift in 1994. Our maximum (and average) estimations from the float measurements collected during the 2016 and 2017 polynyas (within 60% threshold in Table 1), 58.9 (36.1) W m^{-2} and 66.6 (30.7) W m^{-2}, reveal that the oceanic heat flux during a polynya is high compared to the previously observed values. To the best of our knowledge, this is the first estimation of the upper oceanic flux before and during the recent Maud Rise polynyas.

Admittedly, the parameterizations/choices of the above bulk values in Equation 6 require more idealized laboratory experiments and actual field works to better represent the current Weddell Sea or Antarctic research. The largest uncertainty comes from the measurement method itself though: be it from a

mooring, a ship, or a float, all oceanic observations are single profiles. Our results and that of others, for example, Mohrmann et al. (2022), show in contrast a large spatial variability over the polynya region and a daily (or higher) temporal variability. We need observations at a high spatio-temporal resolution, for example, from a flotilla of floats sampling daily, to resolve these scales of variability in the polynya, and more accurately quantify the contribution of the ocean through its life cycle.

5.4. Comparison of the Maud Rise Sea Ice Production to That of Antarctic Coastal Polynyas

Although open-ocean polynyas rarely occur in the Southern Ocean, we find that the ice production within them is comparable to or even more extensive than that in coastal polynyas. Figure 6 compares sea ice production among the 13 major Antarctic coastal polynyas computed by (a) Nihashi and Ohshima (2015) (yellow patches, see their Table 1, average over 2003–2010); (b) Tamura et al. (2008) (green circles, see their Table 1, average over 1992–2001); and (c) Tamura et al. (2016) (purple circles, see their Table 1, average over 1992–2013) to that from our F + O (red and blue patches). There generally exists consistency between production estimations from Nihashi and Ohshima (2015) and Tamura et al. (2008). The differences between three these estimations result from different parameters (i.e., different ρ_{ice} and L_{ice} choices), data sets and spatial coverage. The most considerable contrast is between Nihashi and Ohshima (2015) and Tamura et al. (2016) over the Weddell Sea (W, 271 vs. 38 km^3), as Tamura et al. (2016) integrated ice production in coastal polynyas along an extensive stretch of coastline, while most of them are labeled as fast ice and hence excluded by Nihashi and Ohshima (2015). There, an extra estimation of 155 km^3 from 1992 to 1998 is provided by Renfrew et al. (2002).

There is more agreement at the other coastal polynya locations (Figure 6), highlighting that the Ross Ice Shelf (*R*) polynya is the largest producer (over 300 km^3 sea ice from March to October). We find that the second-largest is the 2017 Maud Rise open-ocean polynya (204.00 km^3), ahead of the Cape Darnley (CD: ∼158 km^3) and Mertz (M: ∼152 km^3) coastal polynyas. Although lower, the sea ice production in the 2016 Maud Rise polynya is nonetheless the eighth highest (87.50 km^3). Therefore, a sizable open-ocean polynya can lead to extensive ice production that is comparable to or even larger than the coastal polynya "ice factories."

High ice production in a coastal polynya can produce dense shelf water (DSW) that contributes to AABW formation (Ohshima et al., 2016). For example, the polynyas by the Ross Ice Shelf and Terra Nova Bay are considered the drivers for Ross Sea Bottom Water production (Comiso et al., 2011; Fusco et al., 2009); sea ice production in the Cape Darnley polynya is directly linked to very saline DSW (>34.8) (Roquet et al., 2013), and the primary DSW source of Cape Darnley bottom water (Ohshima et al., 2013); and the Mertz polynya is identified as the source of Adélie Land Bottom Water (Williams et al., 2008). Therefore, such a large ice production and brine rejection in the open ocean would significantly impact the local stratification and potentially lead to dense water formation (Kusahara et al., 2017). Although Campbell et al. (2019) found no indication of deep convection following the 2016 and 2017 open-ocean polynyas, they did detect "remnants (of) convective plumes," leading them to suspect that deep convection may have taken place but that their 10-daily sampling was too coarse to detect it. Another possibility, as we discussed in Secion 5.2, is that the thermodynamically driven melting of ice within the open-ocean polynya may cause enough restratification to impede convective mixing and AABW formation. Either way, more sensitivity modeling studies and observational campaigns are needed to answer this question.

6. Conclusions

We estimate sea ice production within the 2016/2017 large Maud Rise open-ocean polynyas from the sea ice surface energy budget computed from the CERES-SYN satellite product and JRA55 atm reanalysis. We show that this thermodynamics contribution dominates ice growth and production. For the first time, we also incorporate the oceanic flux into the heat balance, which is evaluated from direct observations collected by drifting profilers. This oceanic heat flux is 36.08 (30.72) Wm^{-2} within the 2016 (2017) open-ocean polynya, on average.

We find large volumes of ice produced in these two polynyas, especially in September 2017 when the open-ocean polynya was largest. We find that the accumulated volume of 2017, 198 km^3, is the second-largest compared to the 13 main Antarctic coastal polynyas (Figure 6). Consistent with the formation mechanism of open-ocean/sensible heat polynya, we find that the daily ice production is most correlated to the skin temperature but only weakly correlated to winds, further showing that these polynya events are primarily controlled by ice thermodynamics

processes. In addition, we found significant sensitivities of the sea ice volume calculation to the 1,000 hPa air temperature, SIC products, wind speed, skin temperature, and polynya threshold. These could explain why polynyas are so poorly represented in climate models (Mohrmann et al., 2021): the atmosphere, sea ice, and ocean diagnostics need to be accurate simultaneously. Our results suggest that the rarely occurring but extensive open-ocean polynyas can result in substantial ice production. They further suggest that as long as the ice remains within the polynya, it can go through cycles of growth and melt processes, that is, re-stabilize the water column, which hinders open-ocean deep convection and deep water formation. However, more observations and model studies are needed to fully understand the above processes, which is challenging as both sea ice and open-ocean deep convection are poorly represented in current climate models (Heuzé, 2021). High-resolution models perform better (Kaufman et al., 2020), but modeling and observation studies, including this one, remain limited as lateral and bottom ice melting cannot be directly estimated from the heat flux (Nihashi et al., 2012). These atmosphere-ice-ocean interactions and their variability in polynyas urgently need to be better understood and disentangled, especially for deep ocean ventilation, AABW formation, and carbon sequestration (Bernardello et al., 2014) given the increasingly vital role of polar processes on the global climate system.

Still, more in-situ observations and model studies need to be combined to explain (a) the detailed feedback between the ocean, ice, and air above polynyas; (b) how ice production responds to the pan-Antarctic open-ocean polynya and influences the local atmosphere circulation and deep convection; and (c) how polynya heat loss influences local/high-latitude climate variability. Fortunately, more specifically designed satellites such as the Ice, Cloud, and Land Elevation Satellite (ICESat)-second-generation ICESat (ICESat-2) (Xu et al., 2021) and the CryoSat-2 (Kacimi & Kwok, 2020) are coming. They will allow for a more realistic detection of sea ice distributions and even snow cover parameters and help to answer the far-reaching consequences of extensive open-ocean polynya activity for the global ocean circulation and ice sheet mass balance with climate change.

Data Availability Statement

The ASI AMSR2 sea ice concentration (SIC) data sets (Melsheimer & Spreen, 2019; Spreen et al., 2008) are available from the Bremen University data center: https://seaice.uni-bremen.de/data. The NASA Team (DiGirolamo et al., 2022) and Bootstrap algorithm (Comiso, 2017) SIC data sets are available from NSIDC: https://n5eil01u.ecs.nsidc.org/PM/NSIDC-0051.002/. The measurements from the two profiling floats were downloaded from the SOCCOM quality-controlled archive (Johnson et al., 2017): http://library.ucsd.edu/dc/collection/bb4473712z. The sea ice thickness from SMOS (Huntemann et al., 2014) and SMOS-SMAP (Paţilea et al., 2019) is provided by Bremen University at https://seaice.uni-bremen.de/databrowser/. ERA5 reanalysis data are from the European Centre for Medium Range Weather Forecast (ECMWF), available via https://cds.climate.copernicus.eu/cdsapp#!/dataset/reanalysis-era5-single-levels. The hourly Modern-Era Retrospective analysis for Research and Applications version 2 (MERRA-2) data sets are available via https://goldsmr4.gesdisc.eosdis.nasa.gov/data/MERRA2/M2T1NXSLV.5.12.4/ The 3-hourly Japanese 55-year Reanalysis (JRA55) are available via: https://rda.ucar.edu/datasets/ds628.0/ The hourly NCEP Climate Forecast System Version 2 (CFSv2) are available via https://rda.ucar.edu/datasets/ds094.1/. The radiative fluxes data sets from CERES and GEO-Enhanced top of the atmosphere, Within-Atmosphere and Surface Fluxes, Clouds and Aerosols Daily Terra-Aqua Edition4A [CER_SYN1DEG-DAY_TERRA-AQUA-MODIS_EDITION4A]. NASA Langley Atmospheric Science Data Center DAAC. Retrieved from https://doi.org/10.5067/Terra+Aqua/CERES/SYN1degDay_L3.004A. The surface ocean current data sets from GLORYS [GLOBAL_REANALYSIS_PHY_001_031] can be access provided by Copernicus Marine Environment Monitoring Service (CMEMS) via: https://doi.org/10.48670/moi-00024. The Sentinel-3A STM (SRAL/MWR) Level 2 sea ice freeboard can be access via https://apihub.copernicus.eu/apihub.

Acknowledgments
Funding for this work was provided by the Swedish National Space Agency, Grant 164/18 awarded to C.H. The authors would like to thank Birte Gülk and Dr. Aditya Narayanan from the Department of Marine Sciences, University of Gothenburg, Sweden; Dr. Malin Ödalen from GEOMAR Helmholtz-Zentrum für Ozeanforschung Kiel, Ocean Circulation and Climate Dynamics, Kiel, Germany; Dr. Stefanie Arndt from the Alfred Wegener Institute, Bremerhaven, Germany; and Julia Kukulies and Hui-Wen Lai from the Department of Earth Sciences, University of Gothenburg, Sweden, for their help with our data questions. The authors would like to thank the two anonymous reviewers for their constructive suggestions.

References

Ackley, S., Perovich, D., Maksym, T., Weissling, B., & Xie, H. (2020). Surface flooding of Antarctic summer sea ice. *Annals of Glaciology*, *61*(82), 117–126. https://doi.org/10.1017/aog.2020.22

Andreas, E. L., Horst, T. W., Grachev, A. A., Persson, P. O. G., Fairall, C. W., Guest, P. S., & Jordan, R. E. (2010a). Parametrizing turbulent exchange over summer sea ice and the marginal ice zone. *Quarterly Journal of the Royal Meteorological Society*, *136*(649), 927–943. https://doi.org/10.1002/qj.618

Andreas, E. L., Persson, P. O. G., Grachev, A. A., Jordan, R. E., Horst, T. W., Guest, P. S., & Fairall, C. W. (2010b). Parameterizing turbulent exchange over sea ice in winter. *Journal of Hydrometeorology*, *11*(1), 87–104. https://doi.org/10.1175/2009JHM1102.1

Barber, D. G., & Massom, R. A. (2007). The role of sea ice in Arctic and Antarctic polynyas. *Elsevier Oceanography Series*, *74*, 1–54. https://doi.org/10.1016/S0422-9894(06)74001-6

Bernardello, R., Marinov, I., Palter, J. B., Galbraith, E. D., & Sarmiento, J. L. (2014). Impact of Weddell Sea deep convection on natural and anthropogenic carbon in a climate model. *Geophysical Research Letters*, *41*(20), 7262–7269. https://doi.org/10.1002/2014GL061313

Boisvert, L. N., Boeke, R. C., Taylor, P. C., & Parker, C. L. (2022). Constraining arctic climate projections of wintertime warming with surface turbulent flux observations and representation of surface-atmosphere coupling. *Frontiers of Earth Science*, *10*. https://doi.org/10.3389/feart.2022.765304

Boisvert, L. N., Markus, T., & Vihma, T. (2013). Moisture flux changes and trends for the entire Arctic in 2003–2011 derived from EOS Aqua data. *Journal of Geophysical Research: Oceans*, *118*(10), 5829–5843. https://doi.org/10.1002/jgrc.20414

Boisvert, L. N., Vihma, T., & Shie, C.-L. (2020). Evaporation from the Southern Ocean estimated on the basis of AIRS satellite data. *Journal of Geophysical Research: Atmospheres*, *125*(1), e2019JD030845. https://doi.org/10.1029/2019JD030845

Boisvert, L. N., Wu, D., Vihma, T., & Susskind, J. (2015). Verification of air/surface humidity differences from AIRS and ERA-Interim in support of turbulent flux estimation in the Arctic. *Journal of Geophysical Research: Atmospheres*, *120*(3), 945–963. https://doi.org/10.1002/2014JD021666

Campbell, E. C., Wilson, E. A., Moore, G. K., Riser, S. C., Brayton, C. E., Mazloff, M. R., & Talley, L. D. (2019). Antarctic offshore polynyas linked to Southern Hemisphere climate anomalies. *Nature*, *570*(7761), 319–325. https://doi.org/10.1038/s41586-019-1294-0

Carsey, F. (1980). Microwave observation of the Weddell Polynya. *Monthly Weather Revie*w, *108*(12), 2032–2044. https://doi.org/10.1175/1520-0493(1980)108⟨2032:MOOTWP⟩2.0.CO;2

Cheng, Z., Pang, X., Zhao, X., & Tan, C. (2017). Spatio-temporal variability and model parameter sensitivity analysis of ice production in Ross Ice Shelf Polynya from 2003 to 2015. *Remote Sensing*, *9*(9), 934. https://doi.org/10.3390/rs9090934

Cheon, W. G., & Gordon, A. L. (2019). Open-ocean polynyas and deep convection in the Southern Ocean. *Scientific Report*s, 9(1), 1–9. https://doi.org/10.1038/s41598-019-43466-2

Comiso, J. C. (2017). *Bootstrap sea ice concentrations from Nimbus-7 SMMR and DMSP SSM/I-SSMIS, version 3*. NASA National Snow and Ice Data Center Distributed Active Archive Center. https://doi.org/10.5067/7Q8HCCWS4I0R

Comiso, J. C., Kwok, R., Martin, S., & Gordon, A. L. (2011). Variability and trends in sea ice extent and ice production in the Ross Sea. *Journal of Geophysical Research*, *116*(C4), C04021. https://doi.org/10.1029/2010JC006391

Cornish, S., Johnson, H., Mallett, R., Dörr, J., Kostov, Y., & Richards, A. (2022). Rise and fall of sea ice production in the Arctic Ocean's ice factories. *Nature Communications*, *13*(1), 7800. https://doi.org/10.1038/s41467-022-34785-6

de Boyer Montégut, C., Madec, G., Fischer, A. S., Lazar, A., & Iudicone, D. (2004). Mixed layer depth over the global ocean: An examination of profile data and a profile-based climatology. *Journal of Geophysical Research*, *109*(C12), C12003. https://doi.org/10.1029/2004JC002378

DiGirolamo, N., Parkinson, C. L., Cavalieri, D. J., Gloersen, P., & Zwally, H. J. (2022). *Sea ice concentrations from Nimbus-7 SMMR and DMSP SSM/I-SSMIS passive microwave data, version 2*. NASA National Snow and Ice Data Center Distributed Active Archive Center. https://doi.org/10.5067/MPYG15WAA4WX

Doelling, D. R., Loeb, N. G., Keyes, D. F., Nordeen, M. L., Morstad, D., Nguyen, C., et al. (2013). Geostationary enhanced temporal interpolation for CERES flux products. *Journal of Atmospheric and Oceanic Technology*, *30*(6), 1072–1090. https://doi.org/10.1175/JTECH-D-12-00136.1

Doelling, D. R., Sun, M., Nguyen, L. T., Nordeen, M. L., Haney, C. O., Keyes, D. F., & Mlynczak, P. E. (2016). Advances in geostationary-derived longwave fluxes for the CERES synoptic (SYN1deg) product. *Journal of Atmospheric and Oceanic Technology*, *33*(3), 503–521. https://doi.org/10.1175/JTECH-D-15-0147.1

d'Ortenzio, F., Iudicone, D., de Boyer Montegut, C., Testor, P., Antoine, D., Marullo, S., et al. (2005). Seasonal variability of the mixed layer depth in the Mediterranean Sea as derived from in situ profiles. *Geophysical Research Letters*, *32*(12), L12605. https://doi.org/10.1029/2005GL022463

Drucker, R., Martin, S., & Kwok, R. (2011). Sea ice production and export from coastal polynyas in the Weddell and Ross Seas. *Geophysical Research Letters*, *38*(17), L17502. https://doi.org/10.1029/2011GL048668

Dufour, C. O., Morrison, A. K., Griffies, S. M., Frenger, I., Zanowski, H., & Winton, M. (2017). Preconditioning of the Weddell Sea polynya by the ocean mesoscale and dense water overflows. *Journal of Climate*, *30*(19), 7719–7737. https://doi.org/10.1175/JCLI-D-16-0586.1

EUMETSAT. (2021). S3IPF – Product data format specification – SRAL and MWR level 2 marine. Retrieved from https://www.eumetsat.int/

Filipponi, F. (2019). Sentinel-1 GRD preprocessing workflow. *Multidisciplinary Digital Publishing Institute Proceeding*s, *18*(1), 11. https://doi.org/10.3390/ECRS-3-06201

Francis, D., Eayrs, C., Cuesta, J., & Holland, D. (2019). Polar cyclones at the origin of the reoccurrence of the Maud Rise Polynya in austral winter 2017. *Journal of Geophysical Research: Atmospheres*, *124*(10), 5251–5267. https://doi.org/10.1029/2019JD030618

Francis, D., Mattingly, K. S., Temimi, M., Massom, R., & Heil, P. (2020). On the crucial role of atmospheric rivers in the two major Weddell Polynya events in 1973 and 2017 in Antarctica. *Science Advances*, *6*(46), eabc2695. https://doi.org/10.1126/sciadv.abc2695

Fu, Q., & Liou, K. (1992). On the correlated k-distribution method for radiative transfer in nonhomogeneous atmospheres. *Journal of the Atmospheric Sciences*, *49*(22), 2139–2156. https://doi.org/10.1175/1520-0469(1992)049⟨2139:OTCDMF⟩2.0.CO;2

Fusco, G., Budillon, G., & Spezie, G. (2009). Surface heat fluxes and thermohaline variability in the Ross Sea and in Terra Nova Bay polynya. *Continental Shelf Research*, *29*(15), 1887–1895. https://doi.org/10.1016/j.csr.2009.07.006

Garric, G., & Parent, L. (2018). Product user manual for global ocean reanalysis products GLOBAL-REANALYSIS-PHY-001-025 (Tech. Rep.). Retrieved from http://cmems-resources.cls.fr/documents/PUM/CMEMS-GLO-PUM-001-025-011-017.pdf

Gelaro, R., McCarty, W., Suárez, M. J., Todling, R., Molod, A., Takacs, L., et al. (2017). The modern-era retrospective analysis for research and applications, version 2 (MERRA-2). *Journal of Climate*, *30*(14), 5419–5454. https://doi.org/10.1175/JCLI-D-16-0758.1

Gordon, A. (1982). Weddell deep water variability. *Journal of Marine Research*, *40*, 199–217.

Gordon, A. L., & Huber, B. A. (1990). Southern Ocean winter mixed layer. *Journal of Geophysical Researc*h, *95*(C7), 11655–11672. https://doi.org/10.1029/JC095iC07p11655

Gordon, A. L., Visbeck, M., & Comiso, J. C. (2007). A possible link between the Weddell Polynya and the Southern Annular Mode. *Journal of Climate*, *20*(11), 2558–2571. https://doi.org/10.1175/JCLI4046.1

Grachev, A. A., Andreas, E. L., Fairall, C. W., Guest, P. S., & Persson, P. O. G. (2007). SHEBA flux–profile relationships in the stable atmospheric boundary layer. *Boundary-Layer Meteorology*, *124*(3), 315–333. https://doi.org/10.1007/s10546-007-9177-6

Guo, G., Shi, J., Gao, L., Tamura, T., & Williams, G. D. (2019). Reduced sea ice production due to upwelled oceanic heat flux in Prydz Bay, East Antarctica. *Geophysical Research Letters*, *46*(9), 4782–4789. https://doi.org/10.1029/2018GL081463

Haid, V., & Timmermann, R. (2013). Simulated heat flux and sea ice production at coastal polynyas in the southwestern Weddell Sea. *Journal of Geophysical Research: Oceans*, *118*(5), 2640–2652. https://doi.org/10.1002/jgrc.20133

Hersbach, H., Bell, B., Berrisford, P., Hirahara, S., Horányi, A., Muñoz-Sabater, J., et al. (2020). The ERA5 global reanalysis. *Quarterly Journal of the Royal Meteorological Society*, *146*(730), 1999–2049. https://doi.org/10.1002/qj.3803

Heuzé, C. (2021). Antarctic bottom water and North Atlantic deep water in CMIP6 models. *Ocean Science*, *17*(1), 59–90. https://doi.org/10.5194/os-17-59-2021

Heuzé, C., Zhou, L., Mohrmann, M., & Lemos, A. (2021). Spaceborne infrared imagery for early detection of Weddell Polynya opening. *The Cryosphere*, *15*(7), 3401–3421. https://doi.org/10.5194/tc-15-3401-2021

Holland, D. (2001). Explaining the Weddell Polynya–a large ocean eddy shed at Maud Rise. *Science*, *292*(5522), 1697–1700. https://doi.org/10.1126/science.1059322

Holland, D. M. (2000). Transient sea-ice polynya forced by oceanic flow variability. *Progress in Oceanography*, *48*(4), 403–460. https://doi.org/10.1016/S0079-6611(01)00010-6

Holland, P. R., & Kwok, R. (2012). Wind-driven trends in Antarctic sea-ice drift. *Nature Geoscience*, *5*(12), 872–875. https://doi.org/10.1038/ngeo1627

Holte, J., & Talley, L. (2009). A new algorithm for finding mixed layer depths with applications to Argo data and Subantarctic Mode Water formation. *Journal of Atmospheric and Oceanic Technology*, *26*(9), 1920–1939. https://doi.org/10.1175/2009JTECHO543.1

Hunke, E., Lipscomb, W., Jones, P., Turner, A., Jeffery, N., & Elliott, S. (2017). *CICE, the Los Alamos sea ice model* (Tech. Rep.). Los Alamos National Lab. (LANL).

Huntemann, M., Heygster, G., Kaleschke, L., Krumpen, T., Mäkynen, M., & Drusch, M. (2014). Empirical sea ice thickness retrieval during the freeze-up period from SMOS high incident angle observations. *The Cryosphere*, *8*(2), 439–451. https://doi.org/10.5194/tc-8-439-2014

Huot, P.-V., Kittel, C., Fichefet, T., Jourdain, N. C., Sterlin, J., & Fettweis, X. (2021). Effects of the atmospheric forcing resolution on simulated sea ice and polynyas off Adélie Land, East Antarctica. *Ocean Modelling*, *168*, 101901. https://doi.org/10.1016/j.ocemod.2021.101901

Jardon, F. P., Vivier, F., Bouruet-Aubertot, P., Lourenço, A., Cuypers, Y., & Willmes, S. (2014). Ice production in Storfjorden (Svalbard) estimated from a model based on AMSR-E observations: Impact on water mass properties. *Journal of Geophysical Research: Oceans*, *119*(1), 377–393. https://doi.org/10.1002/2013JC009322

Jena, B., Ravichandran, M., & Turner, J. (2019). Recent reoccurrence of large open-ocean polynya on the Maud Rise seamount. *Geophysical Research Letters*, *46*(8), 4320–4329. https://doi.org/10.1029/2018GL081482

Johnson, K. S., Riser, S. C., Boss, E. S., Talley, L. D., Sarmiento, J. L., Swift, D. D., et al. (2017). Southern ocean carbon and climate observations and modeling (SOCCOM) float data archive [Dataset]. UC San Diego Library Digital Collections. https://doi.org/10.6075/J0TX3C9X

Kacimi, S., & Kwok, R. (2020). The Antarctic sea ice cover from ICESat-2 and CryoSat-2: Freeboard, snow depth, and ice thickness. *The Cryosphere*, *14*(12), 4453–4474. https://doi.org/10.5194/tc-14-4453-2020

Kaufman, Z. S., Feldl, N., Weijer, W., & Veneziani, M. (2020). Causal interactions between Southern Ocean polynyas and high-latitude atmosphere–ocean variability. *Journal of Climate*, *33*(11), 4891–4905. https://doi.org/10.1175/JCLI-D-19-0525.1

Kern, S., Lavergne, T., Notz, D., Pedersen, L. T., Tonboe, R. T., Saldo, R., & Sørensen, A. M. (2019). Satellite passive microwave sea-ice concentration data set intercomparison: Closed ice and ship-based observations. *The Cryosphere*, *13*(12), 3261–3307. https://doi.org/10.5194/tc-13-3261-2019

Kobayashi, S., Ota, Y., Harada, Y., Ebita, A., Moriya, M., Onoda, H., et al. (2015). The JRA-55 reanalysis: General specifications and basic characteristics. *Journal of the Meteorological Society of Japan. Series II*, *93*(1), 5–48. https://doi.org/10.2151/jmsj.2015-001

Kusahara, K., Williams, G. D., Tamura, T., Massom, R., & Hasumi, H. (2017). Dense shelf water spreading from Antarctic coastal polynyas to the deep Southern Ocean: A regional circumpolar model study. *Journal of Geophysical Research: Oceans*, *122*(8), 6238–6253. https://doi.org/10.1002/2017JC012911

Launiainen, J., & Vihma, T. (1990). Derivation of turbulent surface fluxes – An iterative flux-profile method allowing arbitrary observing heights. *Environmental Software*, *5*(3), 113–124. https://doi.org/10.1016/0266-9838(90)90021-W

Lavergne, T., Piñol Solé, M., Down, E., & Donlon, C. (2021). Towards a swath-to-swath sea-ice drift product for the Copernicus Imaging Microwave Radiometer mission. *The Cryosphere*, *15*(8), 3681–3698. https://doi.org/10.5194/tc-15-3681-2021

Lei, R., Li, Z., Cheng, B., Zhang, Z., & Heil, P. (2010). Annual cycle of landfast sea ice in Prydz Bay, east Antarctica. *Journal of Geophysical Research*, *115*(C2), C02006. https://doi.org/10.1029/2008JC005223

Lellouche, J.-M., Le Galloudec, O., Drévillon, M., Régnier, C., Greiner, E., Garric, G., et al. (2013). Evaluation of global monitoring and forecasting systems at Mercator Océan. *Ocean Science*, *9*(1), 57–81. https://doi.org/10.5194/os-9-57-2013

Lindsay, R., Holland, D., & Woodgate, R. (2004). Halo of low ice concentration observed over the Maud Rise seamount. *Geophysical Research Letters*, *31*(13), L13302. https://doi.org/10.1029/2004GL019831

Ludwig, V., Spreen, G., Haas, C., Istomina, L., Kauker, F., & Murashkin, D. (2019). The 2018 North Greenland polynya observed by a newly introduced merged optical and passive microwave sea-ice concentration dataset. *The Cryosphere*, *13*(7), 2051–2073. https://doi.org/10.5194/tc-13-2051-2019

Lytle, V., & Ackley, S. (1996). Heat flux through sea ice in the western Weddell Sea: Convective and conductive transfer processes. *Journal of Geophysical Research*, *101*(C4), 8853–8868. https://doi.org/10.1029/95JC03675

Macdonald, G. J., Ackley, S. F., & Mestas-Nuñez, A. M. (2022). Evolution of the dynamics, area and ice production of the Amundsen Sea Polynya, Antarctica, 2016–2021. *The Cryosphere Discussions*, 1–32. https://doi.org/10.5194/tc-2022-51

Marsland, S., & Wolff, J.-O. (2001). On the sensitivity of Southern Ocean sea ice to the surface freshwater flux: A model study. *Journal of Geophysical Research*, *106*(C2), 2723–2741. https://doi.org/10.1029/2000JC900086

Martin, S., Drucker, R. S., & Kwok, R. (2007). The areas and ice production of the western and central Ross Sea polynyas, 1992–2002, and their relation to the B-15 and C-19 iceberg events of 2000 and 2002. *Journal of Marine Systems*, *68*(1–2), 201–214. https://doi.org/10.1016/j.jmarsys.2006.11.008

Martin, T., Park, W., & Latif, M. (2013). Multi-centennial variability controlled by Southern Ocean convection in the Kiel Climate Model. *Climate Dynamics*, *40*(7), 2005–2022. https://doi.org/10.1007/s00382-012-1586-7

Maykut, G., & McPhee, M. G. (1995). Solar heating of the Arctic mixed layer. *Journal of Geophysical Research*, *100*(C12), 24691–24703. https://doi.org/10.1029/95JC02554

McDougall, T., & Barker, P. (2011). Getting started with TEOS-10 and the Gibbs Seawater (GSW) Oceanographic toolbox. *Scor/Iapso WG*, *127*(532), 1–28.

Mchedlishvili, A., Spreen, G., Melsheimer, C., & Huntemann, M. (2022). Weddell Sea polynya analysis using SMOS–SMAP apparent sea ice thickness retrieval. *The Cryosphere*, *16*(2), 471–487. https://doi.org/10.5194/tc-16-471-2022

McPhee, M. G. (1992). Turbulent heat flux in the upper ocean under sea ice. *Journal of Geophysical Research*, *97*(C4), 5365–5379. https://doi.org/10.1029/92JC00239

McPhee, M. G., Kottmeier, C., & Morison, J. H. (1999). Ocean heat flux in the central Weddell Sea during winter. *Journal of Physical Oceanography*, *29*(6), 1166–1179. https://doi.org/10.1175/1520-0485(1999)029⟨1166:OHFITC⟩2.0.CO;2

Melsheimer, C., & Spreen, G. (2019). *AMSR2 ASI sea ice concentration data, Antarctic, version 5.4 (NetCDF) (July 2012–December 2018)*. Pangaea. https://doi.org/10.1594/PANGAEA.898400

Menzel, W. P., Schmit, T. J., Zhang, P., & Li, J. (2018). Satellite-based atmospheric infrared sounder development and applications. *Bulletin of the American Meteorological Society*, *99*(3), 583–603. https://doi.org/10.1175/BAMS-D-16-0293.1

Mohrmann, M., Heuzé, C., & Swart, S. (2021). Southern Ocean polynyas in CMIP6 models. *The Cryosphere*, *15*(9), 4281–4313. https://doi.org/10.5194/tc-15-4281-

Mohrmann, M., Swart, S., & Heuzé, C. (2022). Observed mixing at the flanks of Maud Rise in the Weddell Sea. *Geophysical Research Letters*, *49*(8), e2022GL098036. https://doi.org/10.1029/2022GL098036

Monroe, E. E., Taylor, P. C., & Boisvert, L. N. (2021). Arctic cloud response to a perturbation in sea ice concentration: The north water polynya. *Journal of Geophysical Research: Atmospheres*, *126*(16), e2020JD034409. https://doi.org/10.1029/2020JD034409

Morales Maqueda, M., Willmott, A., & Biggs, N. (2004). Polynya dynamics: A review of observations and modeling. *Reviews of Geophysics*, *42*(1), RG1004. https://doi.org/10.1029/2002RG000116

Nakata, K., Ohshima, K., & Nihashi, S. (2021). Mapping of active frazil for Antarctic coastal polynyas, with an estimation of sea-ice production. *Geophysical Research Letters*, *48*(6), e2020GL091353. https://doi.org/10.1029/2020GL091353

Nicolaus, M., Arndt, S., Hoppmann, M., Krumpen, T., Nicolaus, A., & Bartsch, A. (2017a). *Sea ice drift, surface temperature, and barometric pressure on sea ice from Surface Velocity Profiler measurements*. Alfred Wegener Institute, Helmholtz Centre for Polar and Marine Research. https://doi.org/10.1594/PANGAEA.875652

Nicolaus, M., Hoppmann, M., Arndt, S., Hendricks, S., Kaltein, C., König-Langlo, G., et al. (2017b). *Snow height and air temperature on sea ice from snow buoy measurements*. Alred Wegener Institute, Helmholtz Centre for Polar and Marine Research. https://doi.org/10.1594/PANGAEA.875638

Nihashi, S., & Ohshima, K. I. (2015). Circumpolar mapping of Antarctic coastal polynyas and landfast sea ice: Relationship and variability. *Journal of Climate*, *28*(9), 3650–3670. https://doi.org/10.1175/JCLI-D-14-00369.1

Nihashi, S., Ohshima, K. I., & Kimura, N. (2012). Creation of a heat and salt flux dataset associated with sea ice production and melting in the Sea of Okhotsk. *Journal of Climate*, *25*(7), 2261–2278. https://doi.org/10.1175/JCLI-D-11-00022.1

Ohshima, K. I., Fukamachi, Y., Williams, G. D., Nihashi, S., Roquet, F., Kitade, Y., et al. (2013). Antarctic Bottom Water production by intense sea-ice formation in the Cape Darnley polynya. *Nature Geoscience*, *6*(3), 235–240. https://doi.org/10.1038/ngeo1738

Ohshima, K. I., Nihashi, S., & Iwamoto, K. (2016). Global view of sea-ice production in polynyas and its linkage to dense/bottom water formation. *Geoscience Letters*, *3*(1), 1–14. https://doi.org/10.1186/s40562-016-0045-4

Ou, H. W. (1991). Some effects of a seamount on oceanic flows. *Journal of Physical Oceanography*, *21*(12), 1835–1845. https://doi.org/10.1175/1520-0485(1991)021⟨1835:SEOASO⟩2.0.CO;2

Panofsky, H. A. (1984). *Atmospheric Turbulence: Models and Methods for Engineering Applications* (p. 397). Wiley.

Parmiggiani, F. (2011). Multi-year measurement of Terra Nova Bay winter polynya extents. *The European Physical Journal Plus*, *126*(4), 1–7. https://doi.org/10.1140/epjp/i2011-11039-3

Paţilea, C., Heygster, G., Huntemann, M., & Spreen, G. (2019). Combined SMAP–SMOS thin sea ice thickness retrieval. *The Cryosphere*, *13*(2), 675–691. https://doi.org/10.5194/tc-13-675-2019

Petit, B., & Norro, A. (2000). Seasonal evolution of sea ice and oceanic heat flux in the Weddell Sea. *Journal of Marine Systems*, *27*(1–3), 37–52. https://doi.org/10.1016/S0924-7963(00)00060-9

Preußer, A., Ohshima, K. I., Iwamoto, K., Willmes, S., & Heinemann, G. (2019). Retrieval of wintertime sea ice production in Arctic polynyas using thermal infrared and passive microwave remote sensing data. *Journal of Geophysical Research: Oceans*, *124*(8), 5503–5528. https://doi.org/10.1029/2019JC014976

Renfrew, I. A., King, J. C., & Markus, T. (2002). Coastal polynyas in the southern Weddell Sea: Variability of the surface energy budget. *Journal of Geophysical Research*, *107*(C6), 16–1. https://doi.org/10.1029/2000JC000720

Riihelä, A., Key, J. R., Meirink, J. F., Kuipers Munneke, P., Palo, T., & Karlsson, K.-G. (2017). An intercomparison and validation of satellite-based surface radiative energy flux estimates over the Arctic. *Journal of Geophysical Research: Atmospheres*, *122*(9), 4829–4848. https://doi.org/10.1002/2016JD026443

Riser, S. C., Swift, D., & Drucker, R. (2018). Profiling floats in SOCCOM: Technical capabilities for studying the Southern Ocean. *Journal of Geophysical Research: Oceans*, *123*(6), 4055–4073. https://doi.org/10.1002/2017JC013419

Roquet, F., Wunsch, C., Forget, G., Heimbach, P., Guinet, C., Reverdin, G., et al. (2013). Estimates of the Southern Ocean general circulation improved by animal-borne instruments. *Geophysical Research Letters*, *40*(23), 6176–6180. https://doi.org/10.1002/2013GL058304

Rose, F. G., Rutan, D. A., Charlock, T., Smith, G. L., & Kato, S. (2013). An algorithm for the constraining of radiative transfer calculations to CERES-observed broadband top-of-atmosphere irradiance. *Journal of Atmospheric and Oceanic Technology*, *30*(6), 1091–1106. https://doi.org/10.1175/JTECH-D-12-00058.1

Saha, S., Moorthi, S., Wu, X., Wang, J., Nadiga, S., & Tripp, P. (2014). The NCEP climate forecast system version 2. *Journal of Climate*, *27*(6), 2185–2208. https://doi.org/10.1175/JCLI-D-12-00823.1

Small, R. J., Bacmeister, J., Bailey, D., Baker, A., Bishop, S., Bryan, F., et al. (2014). A new synoptic scale resolving global climate simulation using the Community Earth System Model. *Journal of Advances in Modeling Earth Systems*, *6*(4), 1065–1094. https://doi.org/10.1002/2014MS000363

Spreen, G., Kaleschke, L., & Heygster, G. (2008). Sea ice remote sensing using AMSR-E 89-GHz channels. *Journal of Geophysical Research*, *113*(C2), C02S03. https://doi.org/10.1029/2005JC003384

Swart, S., Campbell, E., Heuze, C., Johnson, K., Lieser, J., Massom, R., & others (2018). Return of the Maud Rise polynya: Climate litmus or sea ice anomaly? [in "state of the climate in 2017"]. *Bulletin of the American Meteorological Society*, *99*(8), S188–S189. https://doi.org/10.1175/2018BAMSStateoftheClimate.1

Szanyi, S., Lukovich, J. V., Barber, D., & Haller, G. (2016). Persistent artifacts in the NSIDC ice motion data set and their implications for analysis. *Geophysical Research Letters*, *43*(20), 10–800. https://doi.org/10.1002/2016GL069799

Tamura, T., Ohshima, K. I., Fraser, A. D., & Williams, G. D. (2016). Sea ice production variability in Antarctic coastal polynyas. *Journal of Geophysical Research: Oceans*, *121*(5), 2967–2979. https://doi.org/10.1002/2015JC011537

Tamura, T., Ohshima, K. I., & Nihashi, S. (2008). Mapping of sea ice production for Antarctic coastal polynyas. *Geophysical Research Letters*, *35*(7), L07606. https://doi.org/10.1029/2007GL032903

Tamura, T., Ohshima, K. I., Nihashi, S., & Hasumi, H. (2011). Estimation of surface heat/salt fluxes associated with sea ice growth/melt in the Southern Ocean. *SOLA*, *7*, 17–20. https://doi.org/10.2151/sola.2011-005

Tang, W., Qin, J., Yang, K., Zhu, F., & Zhou, X. (2021). Does ERA5 outperform satellite products in estimating atmospheric downward longwave radiation at the surface? *Atmospheric Research*, *252*, 105453. https://doi.org/10.1016/j.atmosres.2021.105453

Taylor, P. C., Hegyi, B. M., Boeke, R. C., & Boisvert, L. N. (2018). On the increasing importance of air-sea exchanges in a thawing Arctic: A review. *Atmosphere*, *9*(2), 41. https://doi.org/10.3390/atmos9020041

Thompson, L., Smith, M., Thomson, J., Stammerjohn, S., Ackley, S., & Loose, B. (2020). Frazil ice growth and production during katabatic wind events in the Ross Sea, Antarctica. *The Cryosphere*, *14*(10), 3329–3347. https://doi.org/10.5194/tc-14-3329-2020

Thurman, H. V. (2002). *Essentials of oceanography*. Prentice Hall.

Timmermann, R., Lemke, P., & Kottmeier, C. (1999). Formation and maintenance of a polynya in the Weddell Sea. *Journal of Physical Oceanography*, *29*(6), 1251–1264. https://doi.org/10.1175/1520-0485(1999)029⟨1251:FAMOAP⟩2.0.CO;2

Tschudi, M., Meier, W. N., Stewart, J. S., Fowler, C., & Maslanik, J. (2019). *Polar Pathfinder daily 25 km EASE-grid sea ice motion vectors, version 4*. NASA National Snow and Ice Data Center Distributed Active Archive Center. https://doi.org/10.5067/INAWUWO7QH7B

Tsujino, H., Urakawa, S., Nakano, H., Small, R. J., Kim, W. M., Yeager, S. G., et al. (2018). JRA-55 based surface dataset for driving ocean–sea-ice models (JRA55-do). *Ocean Modelling*, *130*, 79–139. https://doi.org/10.1016/j.ocemod.2018.07.002

Untersteiner, N., Thorndike, A., Rothrock, D., & Hunkins, K. (2007). AIDJEX revisited: A look back at the US-Canadian arctic ice dynamics joint experiment 1970–78. *Arctic*, *60*(3), 327–336. https://doi.org/10.14430/arctic233

von Albedyll, L., Hendricks, S., Grodofzig, R., Krumpen, T., Arndt, S., Belter, H. J., et al. (2022). Thermodynamic and dynamic contributions to seasonal Arctic sea ice thickness distributions from airborne observations. *Elementa: Science of the Anthropocene*, *10*(1), 00074. https://doi.org/10.1525/elementa.2021.00074

Walkington, I., & Willmott, A. (2006). A coupled coastal polynya–atmospheric boundary layer model. *Journal of Physical Oceanography*, *36*(5), 897–913. https://doi.org/10.1175/JPO2901.1

Weijer, W., Veneziani, M., Stössel, A., Hecht, M. W., Jeffery, N., Jonko, A., et al. (2017). Local atmospheric response to an open-ocean polynya in a high-resolution climate model. *Journal of Climate*, *30*(5), 1629–1641. https://doi.org/10.1175/JCLI-D-16-0120.1

West, A., Collins, M., Blockley, E., Ridley, J., & Bodas-Salcedo, A. (2019). Induced surface fluxes: A new framework for attributing Arctic sea ice volume balance biases to specific model errors. *The Cryosphere*, *13*(7), 2001–2022. https://doi.org/10.5194/tc-13-2001-2019

Wetzel, P., Haak, H., Jungclaus, J., & Maier-Reimer, E. (2004). The Max-Planck-Institute Global Ocean/Sea-Ice Model (Tech. Rep.). Retrieved from https://mpimet.mpg.de/fileadmin/models/MPIOM/DRAFT_MPIOM_TECHNICAL_REPORT.pdf

Williams, G., Bindoff, N., Marsland, S., & Rintoul, S. (2008). Formation and export of dense shelf water from the Adélie Depression, East Antarctica. *Journal of Geophysical Research*, *113*(C4), C04039. https://doi.org/10.1029/2007JC004346

Wilson, E. A., Riser, S. C., Campbell, E. C., & Wong, A. P. (2019). Winter upper-ocean stability and ice–ocean feedbacks in the sea ice–covered southern ocean. *Journal of Physical Oceanography*, *49*(4), 1099–1117. https://doi.org/10.1175/JPO-D-18-0184.1

Wu, X., Budd, W., & Allison, I. (2003). Modelling the impacts of persistent Antarctic polynyas with an atmosphere–sea-ice general circulation model. *Deep Sea Research Part II: Topical Studies in Oceanography*, *50*(8–9), 1357–1372. https://doi.org/10.1016/S0967-0645(03)00072-9

Xu, Y., Li, H., Liu, B., Xie, H., & Ozsoy-Cicek, B. (2021). Deriving Antarctic sea-ice thickness from satellite altimetry and estimating consistency for NASA's ICESat/ICESat-2 Missions. *Geophysical Research Letters*, *48*(20), e2021GL093425. https://doi.org/10.1029/2021GL093425

Yao, T., & Tang, C. (2003). The formation and maintenance of the North Water Polynya. *Atmosphere-Ocean*, *41*(3), 187–201. https://doi.org/10.3137/ao.410301

Yu, Y., & Rothrock, D. (1996). Thin ice thickness from satellite thermal imagery. *Journal of Geophysical Research*, *101*(C11), 25753–25766. https://doi.org/10.1029/96JC02242

Zhou, L., Heuzé, C., & Mohrmann, M. (2022). Early winter triggering of the Maud Rise Polynya. *Geophysical Research Letters*, *49*(2), e2021GL096246. https://doi.org/10.1029/2021GL096246

References From the Supporting Information

Lebedev, V. (1938). Rost l'da v arkticheskikh rekakh i moriakh v zavisimosti ot otritsatel'nykh temperatur vozdukha. *Problemy arktiki*, *5*(6), 9–25.

Maykut, G. A. (1986). The surface heat and mass balance. In *The geophysics of sea ice* (pp. 395–463). Springer. https://doi.org/10.1007/978-1-4899-5352-06